



Translational two-pore PBPK model to characterize whole-body disposition of different-size endogenous and exogenous proteins

Shufang Liu¹ · Yingyi Li¹ · Zhe Li¹ · Shengjia Wu¹ · John M. Harrold² · Dhaval K. Shah¹

Received: 10 January 2024 / Accepted: 19 April 2024 / Published online: 1 May 2024

© The Author(s), under exclusive licence to Springer Science+Business Media, LLC, part of Springer Nature 2024

Abstract

Two-pore physiologically based pharmacokinetic (PBPK) modeling has demonstrated its potential in describing the pharmacokinetics (PK) of different-size proteins. However, all existing two-pore models lack either diverse proteins for validation or interspecies extrapolation. To fill the gap, here we have developed and optimized a translational two-pore PBPK model that can characterize plasma and tissue disposition of different-size proteins in mice, rats, monkeys, and humans. Datasets used for model development include more than 15 types of proteins: IgG (150 kDa), F(ab)2 (100 kDa), minibody (80 kDa), Fc-containing proteins (205, 200, 110, 105, 92, 84, 81, 65, or 60 kDa), albumin conjugate (85.7 kDa), albumin (67 kDa), Fab (50 kDa), diabody (50 kDa), scFv (27 kDa), dAb2 (23.5 kDa), proteins with an albumin-binding domain (26, 23.5, 22, 16, 14, or 13 kDa), nanobody (13 kDa), and other proteins (110, 65, or 60 kDa). The PBPK model incorporates: (i) molecular weight (MW)-dependent extravasation through large and small pores via diffusion and filtration, (ii) MW-dependent renal filtration, (iii) endosomal FcRn-mediated protection from catabolism for IgG and albumin-related modalities, and (iv) competition for FcRn binding from endogenous IgG and albumin. The finalized model can well characterize PK of most of these proteins, with area under the curve predicted within two-fold error. The model also provides insights into contribution of renal filtration and lysosomal degradation towards total elimination of proteins, and contribution of paracellular convection/diffusion and transcytosis towards extravasation. The PBPK model presented here represents a cross-modality, cross-species platform that can be used for development of novel biologics.

Keywords Two-pore theory · Physiologically based pharmacokinetic (PBPK) modeling · Protein therapeutics · Monoclonal antibody · Antibody fragments · Albumin

Introduction

The past few decades have witnessed a surge of therapeutic proteins, including the blockbuster monoclonal antibodies (mAbs), antibody fragments such as nanobodies,

single-chain variable fragments (scFv), and bispecific T cell engagers (BiTE) [1], and proteins containing albumin-binding domains (Albuds) that hitchhike on albumin for extended half-life [2, 3]. It is becoming an important strategic question as to what modality should be chosen in different scenarios to achieve desired exposure, clearance, distribution, and target engagement at the site-of-action. To address this question, it would be beneficial to have a unified mathematical modelling platform that can predict the pharmacokinetics (PK) of diverse biologics for different preclinical species and humans.

One such platform is physiologically based pharmacokinetic (PBPK) models, which can characterize drug concentrations in circulation and at the site-of-action, and can be translated from preclinical animals to humans. In PBPK models for biologics, while most physiological parameters such as blood flows and organ volumes are relatively standard and allow convenient cross-species extrapolation,

✉ Shufang Liu
shufangl@buffalo.edu

Dhaval K. Shah
dshah4@buffalo.edu

John M. Harrold
john.harrold@pfizer.com

¹ Department of Pharmaceutical Sciences, School of Pharmacy and Pharmaceutical Sciences, The State University of New York at Buffalo, 455 Pharmacy Building, Buffalo, NY 14214-8033, USA

² Pharmacometrics & Systems Pharmacology, Pfizer Inc, South San Francisco, CA, USA

drug-specific PK parameters are difficult to determine. This is due to the complex physicochemical properties of proteins (e.g., molecular size, charge, glycosylation, shape, rigidity, etc.) that substantially impact their distribution and elimination characteristics [4–7]. Among these molecular attributes, the effect of molecular weight (MW) is the most outstanding and the best understood. With respect to elimination, the relationship between renal clearance and MW is sigmoidal [5, 8], where proteins with MW > 70 kDa can barely pass the glomerular membrane and proteins with MW < 12 kDa can be freely filtered. The extent and kinetics of tissue distribution is negatively correlated with MW [9], which can be mathematically described using the two-pore formalism.

In the two-pore theory proposed by Rippe and Haraldsson [10, 11], continuous and fenestrated endothelium is assumed to contain two categories of pores – large pores (radius ~ 22 nm) and small pores (radius ~ 4 nm). To explain a transvascular influx of proteins in the absence of net lymphatic filtration (i.e., isogravimetric state), an isogravimetric circular flow was hypothesized to enter large pores and exit small pores driven by the osmotic pressure. Protein solutes can extravasate via diffusion and convection through large pores and small pores, which are largely determined by the protein size relative to the vascular pore size. While the first application of the two-pore theory in PBPK modeling of protein therapeutics dates to the 1990s [12], its utility has been very limited until the past decade. One biggest hurdle used to be the unavailability and poor identifiability of two-pore parameters that define diffusion, convection, and the isogravimetric flow. Not only are these parameters hard to measure experimentally, but also model estimated values of these parameters vary greatly among studies [12–15]. This dilemma was addressed in 2015, when Sepp et al. did further derivations and demonstrated that the permeability-surface area product (PS) and the isogravimetric flow rate (J_{iso}) were linear functions of the organ lymph flow rate [16]. Since then, Sepp and colleagues have evolved the two-pore model to characterize whole-body disposition of dAb2, IgG and albumin in mice and rats [17], and subsequently a domain antibody (an Albuld) in humans [18]. Our laboratory also developed and validated a two-pore model with de novo derived parameters for a more diverse panel of protein modalities (13–150 kDa) including IgG, F(ab)2, minibody, scFv2, Fab, scFv, and nanobody in mice [19–21]. As part of the PK-Sim software, the model by Niederalt et al. was also used to capture IgG PK in mice, monkeys, and humans, as well as dAb2 PK in mice and inulin in rats [15].

Our evaluation of these published two-pore model versions highlights another challenge: we have not validated the applicability of these models across species and across protein modalities simultaneously. Usually, the developed models have either been extrapolated across species for only a very limited number of modalities [15, 17], or demonstrated predictability for many proteins in only one species [20]. And among them, only one PBPK version incorporated

albumin [17, 18], an increasingly important protein exploited in many drug development strategies [22, 23]. Moreover, despite the anticipation that such a model should work for all proteins, certain modality- or species-specific modifications that deviate from the two-pore theory are still needed in order to capture the data. But these assumptions are obscured and poorly recognized when models are tested in different publications, as summarized in Table 1.

To address these issues, in this manuscript we aimed to develop and calibrate a so-far most comprehensive two-pore PBPK model based on the foundational work reported previously, utilizing extensive datasets that incorporate whole-body PK data of different-size proteins in preclinical species and humans. This finalized model can be applied to a priori characterize plasma and tissue PK of endogenous albumin and IgG, and exogenously dosed proteins with MW ranging from 13–205 kDa with or without FcRn interactions in four species (i.e., mice, rats, monkeys, and humans).

Methods

PK dataset for model calibration

Plasma and tissue PK data of different-size proteins following intravenous administration in mice, rats, monkeys, and humans were collected from the literature. These proteins incrementally span a wide range of MW with or without FcRn interaction.

Mouse datasets include nanobody (13 kDa), dAb2 (23.5 kDa), Albuld (dAb2) (23.5 kDa), scFv (27 kDa), Fab (50 kDa), diabody (50 kDa), nanobody-PAS600 (60 kDa), mouse albumin (67 kDa), minibody (80 kDa), F(ab)2 (100 kDa), scFv-Fc (105 kDa), TandAb (110 kDa), human IgG1 (150 kDa), FcRn-nonbinding human IgG1 (150 kDa), murine or human IgG1 in FcRn knockout mice, and scFv-IgAb (205 kDa).

Rat datasets include inulin (5.5 kDa, a type of polysaccharide rather than a protein), dAb2 (23.5 kDa), scFv (27 kDa), Fab (50 kDa), nanobody-PAS600 (60 kDa), Fc-fusion proteins (60 and 92 kDa), rat albumin (67 kDa), F(ab)2 (100 kDa), human IgG1 (150 kDa), and FcRn-non-binding human IgG1 (150 kDa).

Monkey datasets include nanobody (13 kDa), Albuld (DARPin) (14 kDa), dAb-Albuld (16 kDa), anticalin-Albuld (22 kDa), nanobody-Albuld (26 kDa), Fab (50 kDa), nanobody-PAS600 (60 kDa), IFN α -human albumin conjugate (85.7 kDa), F(ab)2 (110 kDa), scFv-Fc (110 kDa), human IgG1 (150 kDa), DVD-Ig (200 kDa), and scFv-IgAb (205 kDa).

Human datasets include Albuld (dAb) (13 kDa), Fab (50 kDa), scFv-PE (65 kDa), Fc-fusion proteins (65, 81, 84, and 92 kDa), human albumin (67 kDa), F(ab)2 (100 kDa), and human IgG (150 kDa), as well as human IgG1 (150 kDa) in familial hypercatabolic hypoproteinemia (FHH) patients.

Table 1 Overview of published two-pore PBPK model versions

Reference	Modalities and species	Coherence characteristics
Baxter et al. [24]	• mAb (150 kDa) in <i>mouse and human</i>	<i>Modality/Species-dependent:</i> Reflection coefficients, permeabilities, and renal excretion vary with molecular size and species (fitted)
Baxter et al. [12]	• [sc(Fv)2]2 (120 kDa), F(ab)2 (100 kDa), sc(Fv)2 (60 kDa), and Fab (50 kDa) in <i>mouse</i>	
Ferl et al. [13]		
Davda et al. [14]		
Niederalt et al. [15]	• mAb (150 kDa) in <i>mouse, monkey, and human</i> • dAb2 (25.6 kDa) in <i>mouse</i> • inulin (5.5 kDa) in <i>rat</i>	<i>Species-dependent:</i> FcRn concentrations (fitted) Ratio of recirculation flow rate to lymph flow rate in human is lower (fitted) <i>Modality-dependent:</i> Pinocytosis of inulin set to 0 Sieving coefficients (fitted)
Sepp et al. [16]	• mAb (150 kDa) in <i>mouse and rat</i>	<i>Modality/Species-dependent:</i> Renal sieving coefficient of albumin in human is fivefold lower than in other species
Sepp et al. [17]	• albumin (67 kDa) in <i>mouse, rat, and human</i>	
Sepp et al. [18]	• dAb2 (25.6 kDa) in <i>mouse and rat</i> • Albud dAb2 (25.6 kDa) in <i>mouse</i> • Albud dAb (13 kDa) in <i>human</i>	
Li and Shah [19]	• mAb (150 kDa), F(ab)2 (100 kDa), minibody (80 kDa), scFv2 (55 kDa), Fab (50 kDa), diabody (50 kDa), scFv (27 kDa), and nanobody (13 kDa) in <i>mouse</i>	
Li et al. [20]		
Li et al. [21]		
The present study	• mAb (150 kDa) in <i>mouse, rat, monkey, and human</i> • F(ab)2 (100 kDa) in <i>mouse, rat, monkey, and human</i> • Minibody (80 kDa) in <i>mouse</i> • Fc-fusion proteins (205, 200, 110, 105, 92, 84, 81, 65, or 60 kDa) in <i>mouse, rat, monkey, and human</i> • Albumin-conjugate (85.7 kDa) in <i>monkey</i> • lbumin (67 kDa) in <i>mouse, rat, and human</i> • Fab (50 kDa) in <i>mouse, rat, monkey, and human</i> • Diabody (50 kDa) in <i>mouse</i> • scFv (27 kDa) in <i>mouse and rat</i> • dAb2 (23.5 kDa) in <i>mouse and rat</i> • Albud proteins (26, 23.5, 22, 16, 14, or 13 kDa) in <i>mouse, rat, monkey, and human</i> • Nanobody (13 kDa) in <i>mouse and monkey</i> • Inulin (5.5 kDa) in <i>rat</i> • Other proteins (110, 65, or 60 kDa) in <i>mouse, rat, monkey, and human</i>	<i>Modality/Species-dependent:</i> Pinocytosis of albumin is lower than other higher-pI proteins (fitted)

Supplementary Table 1 provides a full list of all the studies incorporated in the model. Data was digitized using the WebPlotDigitizer 4.6. Blood concentrations were converted to plasma concentrations assuming the hematocrit of 45%. Digitized data was then pooled and dose-normalized to 1 mg/kg dose level for comparison with model outputs. The collected PK data was deemed linear based on one of the following criteria (Supplementary Table 1): (1) There is no target-binding in the species of interest; (2) Multiple dose levels have been tested and PK linearity was verified; (3) The dose level was considered sufficiently high to saturate any potential target binding. When the dose level was not high enough to confidently conclude negligible impact of target binding, PK linearity was assumed with caution if the data was consistent with other linear PK data for proteins with a similar MW or if the data was used in previous publications for linear PBPK model validation.

PBPK model structure and equations

Whole-body level protein transport

The overall PBPK model consists of central plasma, lumped lymph nodes, and 15 organs, including lung, heart, kidney, muscle, skin, liver, brain, adipose, thymus, bone, small intestine, large intestine, spleen, pancreas, and an “other” compartment containing all other tissues not explicitly represented [25] (Fig. 1A). Proteins enter organs via arterial plasma flow (Q_{Org}) and exit via venous plasma flow ($Q_{Org} - J_{Org}$). Lymph flow drives convection from vascular space to interstitial space of an organ and merges into lymphatic circulation ($J_{Org} \cdot (1 - \sigma_{Org}^I)$), which is all collected by the “lymph node” compartment, followed by draining into plasma.

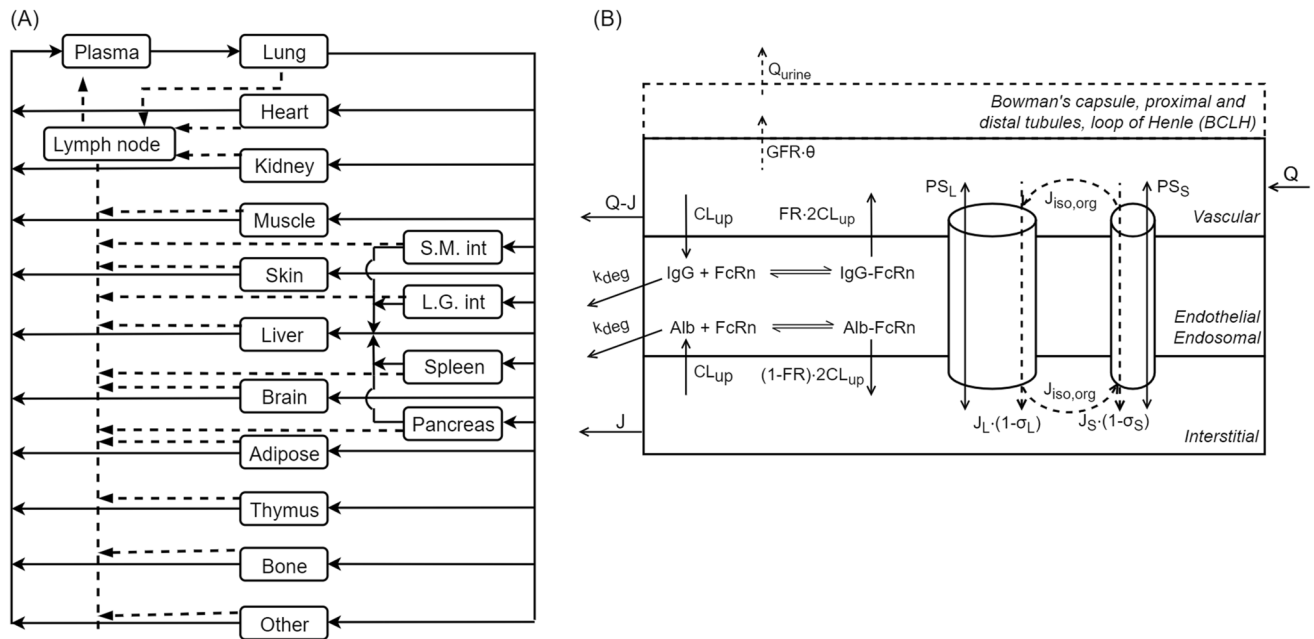


Fig. 1 Schematic of the two-pore PBPK model. **A** Structure of the whole-body level PBPK model. Organs are connected via blood flows (solid arrows) and lymphatic flows (dashed arrows) in an anatomical manner. **B** Structure of the tissue-level PBPK model based on the two-pore hypothesis. Each tissue is comprised of vascular, endothelial endosomal, and interstitial spaces. Vascular proteins can enter tissues via diffusion and convection through large and small pores. An

isogravimetric flow driven by osmotic pressure is included. Vascular and interstitial IgG and albumin can be pinocytosed into endothelial endosomes, where FcRn-bound proteins can be recycled and free proteins are degraded. For kidney, an additional compartment is incorporated that combines Bowman's capsule, proximal and distal tubules, and loop of Henle (BCLH). Renal vascular proteins are filtered into BCLH followed by elimination with urinary flow

In central plasma,

$$V_{\text{Plasma}} \frac{dC_{\text{Plasma}}^{\text{SUB}}}{dt} = \sum_{i=\text{All organs excluding lung, liver, SI, LI, pancreas, spleen}} (Q_i - J_i) \cdot C_i^{\text{V,SUB}} + L_{\text{Lymph}} \cdot C_{\text{Lymph}}^{\text{SUB}} - (Q_{\text{Lung}} + J_{\text{Lung}}) \cdot C_{\text{Plasma}}^{\text{SUB}} + \text{Binding}_{\text{Plasma}}^{\text{SUB}} \cdot V_{\text{Plasma}} + K_{\text{syn,SUB}} \cdot V_{\text{Plasma}} \quad (1)$$

In the lymph nodes,

$$V_{\text{Lymph}} \frac{dC_{\text{Lymph}}^{\text{SUB}}}{dt} = \sum_{i=\text{All organs}} (1 - \sigma_i^I) \cdot J_i \cdot C_i^{I,\text{SUB}} - L_{\text{Lymph}} \cdot C_{\text{Lymph}}^{\text{SUB}} + \text{Binding}_{\text{Lymph}}^{\text{SUB}} \cdot V_{\text{Lymph}} \quad (2)$$

Model equations were coded in a modular fashion. Here, the superscript, “SUB”, refers to endogenous IgG (*enIgG*), endogenous albumin (*enAlb*), exogenous IgG (*exoIgG*), exogenous albumin (*exoAlb*), proteins with an albumin-binding domain (*Albud*), or the complex of the *Albud* protein bound to endogenous albumin (*AlbudAl*). Binding between *Albud* and *enAlb* occurs in liquid compartments including

vascular and interstitial spaces of organs, central plasma, and lymph nodes. For example,

$$\begin{aligned} \text{Binding}_{\text{Plasma}}^{\text{Albud}} &= \text{Binding}_{\text{Plasma}}^{\text{enAlb}} = -\text{Binding}_{\text{Plasma}}^{\text{AlbudAl}} \\ &= -K_{\text{on}}^{\text{Alb,Albud}} \cdot C_{\text{Plasma}}^{\text{Albud}} \cdot C_{\text{Plasma}}^{\text{enAlb}} \\ &\quad + K_{\text{off}}^{\text{Alb,Albud}} \cdot C_{\text{Plasma}}^{\text{AlbudAl}} \end{aligned} \quad (3)$$

Continuous synthesis of endogenous albumin and IgG is added to central plasma. Instead of manually adjusting the values of *K_{syn,SUB}* to match steady-state endogenous protein levels, we implemented the general method for initialization of steady states in complex biological systems introduced by Abuqayyas and Harrold, which has been validated in PBPK models and in systems where one biomarker is upstream of another [26].

In this manner, $K_{syn_{enIgG}}$ and $K_{syn_{enAlb}}$ can be numerically solved in the system stabilization period (equations and results for steady-state determination are detailed in the Supplementary Material), which greatly facilitates the model development process and allows estimation of any parameters that potentially impact disposition of endogenous proteins.

Tissue level protein disposition

Figure 1B displays the tissue level model for protein disposition using the two-pore formalism [10, 11]. Tissue endothelia is considered porous with two categories of pores, large pores (pore radius ~ 22 nm) and small pores (pore radius ~ 4 nm) [11]. Proteins can be passively transported to the interstitial space through both types of pores via diffusion ($PS_{L,Org}^{SUB}$ and $PS_{S,Org}^{SUB}$) or fluid phase convection ($J_{L,Org} \cdot (1 - \sigma_L^{SUB})$ and $J_{S,Org} \cdot (1 - \sigma_S^{SUB})$). Both the permeability-surface area

products (PS) and the vascular reflection coefficients that reflect restriction to protein convection (σ) are molecular size-dependent and pore size-dependent parameters. The isogravitropic flow ($J_{iso,Org}$) driven by osmotic pressure is included. Two-pore uptake clearance of proteins mediated by the above-mentioned paracellular extravasation processes via large and small pores are represented as $CL_{TP,Org,L}^{SUB}$ and $CL_{TP,Org,S}^{SUB}$, respectively. On the other hand, proteins in vascular and interstitial spaces are subjected to fluid phase pinocytosis (CL_{up}^{Org}) into endosomes, where albumin and IgG can bind to FcRn. Unbound endosomal proteins are assumed to be degraded (K_{deg}), and FcRn-bound albumin and Fc-containing proteins are assumed to recycle to vascular ($2CL_{up}^{Org} \cdot FR$) and interstitial ($2CL_{up}^{Org} \cdot (1 - FR)$) spaces. A factor of 2 on CL_{up}^{Org} is needed here so that the exocytosed volume is equal to the total pinocytosed volume from vascular and interstitial spaces per unit time (i.e., $2CL_{up}^{Org} \cdot FR + 2CL_{up}^{Org} \cdot (1 - FR) = CL_{up}^{Org} + CL_{up}^{Org}$).

In vascular space:

$$\begin{aligned} V_{Org}^V \frac{dC_{Org}^{V,SUB}}{dt} &= Mass_{Org}^{VI,SUB} - Mass_{Org}^{VO,SUB} - Spino_{SUB} \cdot CL_{up}^{Org} \cdot C_{Org}^{V,SUB} \\ &\quad + 2CL_{up}^{Org} \cdot FR \cdot C_{Org}^{E,B,SUB} + Binding_{Org}^{V,SUB} \cdot V_{Org}^V \\ &\quad - (CL_{TP,L,Org}^{SUB} + CL_{TP,S,Org}^{SUB}) \cdot C_{Org}^{V,SUB} \end{aligned} \quad (4)$$

In interstitial space:

$$\begin{aligned} V_{Org}^I \frac{dC_{Org}^{I,SUB}}{dt} &= (CL_{TP,L,Org}^{SUB} + CL_{TP,S,Org}^{SUB}) \cdot C_{Org}^{V,SUB} \\ &\quad - (1 - \sigma_{Org}^I) \cdot J_{Org} \cdot C_{Org}^{I,SUB} - Spino_{SUB} \cdot CL_{up}^{Org} \cdot C_{Org}^{I,SUB} \\ &\quad + 2CL_{up}^{Org} \cdot (1 - FR) \cdot C_{Org}^{E,B,SUB} + Binding_{Org}^{I,SUB} \cdot V_{Org}^I \end{aligned} \quad (5)$$

Above, $Spino_{SUB}$ is a modification factor on pinocytosis of "SUB", reflecting the effect of physicochemical properties such as charge on this nonspecific uptake mechanism [27]. In Eq. (4), $Mass_{Org}^{VI,SUB}$ and $Mass_{Org}^{VO,SUB}$ are masses of "SUB" entering and exiting an organ.

For typical organs,

$$Mass_{Org}^{VI,SUB} = Q_{Org} \cdot C_{Lung}^{V,SUB} \quad (6)$$

$$Mass_{Org}^{VO,SUB} = (Q_{Org} - J_{Org}) \cdot C_{Org}^{V,SUB} \quad (7)$$

whereas for lung,

$$Mass_{Lung}^{VI,SUB} = (Q_{Lung} + J_{Lung}) \cdot C_{Plasma}^{SUB} \quad (8)$$

$$Mass_{Lung}^{VO,SUB} = Q_{Lung} \cdot C_{Lung}^{V,SUB} \quad (9)$$

For liver,

$$\begin{aligned} Mass_{Liver}^{VI,SUB} &= Q_{Liver} \cdot C_{Lung}^{V,SUB} \\ &\quad + \sum_{i=Pancreas,SI,LI,spleen} (Q_i - J_i) \cdot C_i^{V,SUB} \end{aligned} \quad (10)$$

$$\begin{aligned} Mass_{Liver}^{VO,SUB} &= ((Q_{Liver} - J_{Liver}) \\ &\quad + \sum_{i=Pancreas,SI,LI,spleen} (Q_i - J_i)) \cdot C_{Liver}^{V,SUB} \end{aligned} \quad (11)$$

In the kidney, renal filtration represents an additional elimination mechanism, which is significant for proteins with MW < 70 kDa:

$$\begin{aligned} Mass_{Kidney}^{VO,SUB} = & (Q_{Kidney} - J_{Kidney}) \cdot C_{Kidney}^{V,SUB} \\ & + GFR \cdot \theta_{SUB} \cdot (1 - Frea_{SUB}) \cdot C_{Kidney}^{V,SUB} \end{aligned} \quad (12)$$

Above, GFR is the glomerular filtration rate, θ_{SUB} is the glomerular sieving coefficient, and $Frea_{SUB}$ is the fraction of proteins reabsorbed. Furthermore, the filtered “ SUB ” in a lumped space combining Bowman’s capsule, proximal and distal tubules, and the loop of Henle (BCLH) is eliminated with urine flow [16]:

$$\begin{aligned} \frac{dA_{BCLH}^{SUB}}{dt} = & GFR \cdot \theta_{SUB} \cdot (1 - Frea_{SUB}) \cdot C_{Kidney}^{V,SUB} \\ & - Q_{urine} \cdot A_{BCLH}^{SUB} / V_{BCLH} \end{aligned} \quad (13)$$

Endosomal processing of proteins

In the endosomal space, IgG and albumin bind to different sites on FcRn (i.e., no competition). Therefore, for simplification of mathematical expression, we created two sets – “ IGG ” that represents either *enIgG* or *exoIgG*, and “ ALB ” that stands for *enAlb*, *exoAlb*, *Albud*, or *AlbudAl*. Only molecules within the same set compete for the same FcRn binding site.

$$\begin{aligned} V_{Org}^E \frac{dC_{Org}^{E,UB,IGG}}{dt} = & Spino_{IGG} \cdot CL_{up}^{Org} \cdot (C_{Org}^{I,IGG} + C_{Org}^{V,IGG}) - K_{on}^{FcRn,IGG} \cdot C_{Org}^{E,UB,IGG} \cdot FcRn_{Org}^{IgG} \cdot V_{Org}^E \\ & + K_{off}^{FcRn,IGG} \cdot C_{Org}^{E,B,IGG} \cdot V_{Org}^E - K_{deg} \cdot C_{Org}^{E,UB,IGG} \cdot V_{Org}^E \end{aligned} \quad (14)$$

$$\begin{aligned} V_{Org}^E \frac{dC_{Org}^{E,UB,ALB}}{dt} = & Spino_{ALB} \cdot CL_{up}^{Org} \cdot (C_{Org}^{I,ALB} + C_{Org}^{V,ALB}) - K_{on}^{FcRn,ALB} \cdot C_{Org}^{E,UB,ALB} \cdot FcRn_{Org}^{Alb} \cdot V_{Org}^E \\ & + K_{off}^{FcRn,ALB} \cdot C_{Org}^{E,B,ALB} \cdot V_{Org}^E - K_{deg} \cdot C_{Org}^{E,UB,ALB} \cdot V_{Org}^E \end{aligned} \quad (15)$$

In essence, Eq. (14) can be expanded to 2 differential equations (for *enIgG* and *exoIgG* respectively), and there

are 4 differential equations underlying Eq. (15) (for *enAlb*, *exoAlb*, *Albud*, and *AlbudAl*, respectively). The same also applies to Eqs. (16) and (17).

$$V_{Org}^E \frac{dC_{Org}^{E,B,IGG}}{dt} = -2CL_{up}^{Org} \cdot C_{Org}^{E,B,IGG} + K_{on}^{FcRn,IGG} \cdot C_{Org}^{E,UB,IGG} \cdot FcRn_{Org}^{IgG} \cdot V_{Org}^E - K_{off}^{FcRn,IGG} \cdot C_{Org}^{E,B,IGG} \cdot V_{Org}^E \quad (16)$$

$$V_{Org}^E \frac{dC_{Org}^{E,B,ALB}}{dt} = -2CL_{up}^{Org} \cdot C_{Org}^{E,B,ALB} + K_{on}^{FcRn,ALB} \cdot C_{Org}^{E,UB,ALB} \cdot FcRn_{Org}^{Alb} \cdot V_{Org}^E - K_{off}^{FcRn,ALB} \cdot C_{Org}^{E,B,ALB} \cdot V_{Org}^E \quad (17)$$

Accordingly, there are two independent pools of free FcRn binding sites – one for Fc binding (Eq. (18)) and the other for albumin binding (Eq. (19)):

$$\begin{aligned} V_{Org}^E \frac{dFcRn_{Org}^{IgG}}{dt} = & \sum_{IGG=enIgG,exoIgG} (2CL_{up}^{Org} \cdot C_{Org}^{E,B,IGG} + K_{off}^{FcRn,IGG} \cdot C_{Org}^{E,B,IGG} \cdot V_{Org}^E - K_{on}^{FcRn,IGG} \cdot C_{Org}^{E,UB,IGG} \cdot FcRn_{Org}^{IgG} \cdot V_{Org}^E) \\ FcRn_{Org}^{IgG}(0) = & FcRn_0^{IgG} \end{aligned} \quad (18)$$

$$V_{Org}^E \frac{dFcRn_{Org}^{Alb}}{dt} = \sum_{\substack{ALB = enAlb, exoAlb, \\ Albud, AlbudAl}} (2CL_{up}^{Org} \cdot C_{Org}^{E,B,ALB} + K_{off}^{FcRn,ALB} \cdot C_{Org}^{E,B,ALB} \cdot V_{Org}^E - K_{on}^{FcRn,ALB} \cdot C_{Org}^{E,UB,ALB} \cdot FcRn_{Org}^{Alb} \cdot V_{Org}^E) \quad (19)$$

$FcRn_{Org}^{Alb}(0) = FcRn_0^{Alb}$

The interaction between albumin and FcRn is in 1:1 stoichiometry [28], in contrast to one IgG molecule binding to two FcRn molecules [29]. As affinities for IgG binding to FcRn already account for avidity, the effective concentration of albumin binding sites on FcRn is twice that for IgG, i.e., $FcRn_0^{Alb} = 2FcRn_0^{IgG}$.

$$a_e^{SUB} = 0.5614 \left(\frac{MW_{SUB}}{1000} \right)^{\frac{1}{3}} + 0.09611 \left(\frac{MW_{SUB}}{1000} \right)^{\frac{2}{3}} \quad (a_e^{SUB} \text{ in nm and } MW_{SUB} \text{ in Dalton}) \quad (20)$$

Two distinct empirical equations have been used to correlate θ_{SUB} and protein size in the past [17, 19]:

$$\theta_{SUB} = \frac{1}{(1 + (\frac{a_e^{SUB}}{2.95})^{7.11})^{3.8}} \quad (Sepp \text{ et al.}) \quad (21)$$

$$\theta_{SUB} = e^{(\frac{8.7}{1 + e^{0.028(-\frac{MW_{SUB}}{1000} + 72.3)}})} \quad (Li \text{ and Shah}) \quad (22)$$

These two relationships yield sieving coefficients that can differ by almost 100 folds for proteins with MW of 60 kDa (Supplementary Figure 3). This is attributed to the fact that these equations were generated or fitted based on different datasets – while Sepp et al. utilized experimentally measured sieving coefficients for neutral proteins and negatively charged albumin [17, 30], Li and Shah referred to the data summarized by Haraldsson et al. for positively charged macromolecules [8, 19]. Because of dense

Molecular size-dependent relationships

The hydrodynamic radius of a protein (a_e^{SUB}) is calculated using the equation shown below, as reported by Sepp et al. based on the relationship between the experimentally measured Stokes radius and MW for proteins ranging from 6.4 to 440 kDa [16].

negatively charge glycosaminoglycans on the glomerular basement membrane, negatively charged proteins are less likely to be filtered [31]. Consequently, θ for positively charged proteins is much higher than that for neutral and negatively charged proteins. We have tested both relationships during the model optimization stage and eventually adopted the former one (i.e., Eq. (21)) in the final version of the model, because it well characterizes the greater majority of the modalities including the albumin. But chances are that the latter relationship (Eq. (22)) works better for certain modalities in the current modeling framework (as described in Results and Discussion sections).

The following two-pore representations are based on the formalism proposed by Rippe and Haraldsson [10, 11], important derivations by Sepp et al. [16], and further expansions and simplifications by Li and Shah [19].

Two-pore clearance of proteins via large and small pores are expressed using Patlak equation [32]:

$$CL_{TP,L,Org}^{SUB} = PS_{L,Org}^{SUB} \cdot \left(1 - \frac{C_{Org}^{I,SUB}}{C_{Org}^{V,SUB}} \right) \cdot \frac{Pe_{L,Org}^{SUB}}{e^{Pe_{L,Org}^{SUB}} - 1} + J_{L,Org} \cdot (1 - \sigma_L^{SUB}) \quad (23)$$

$$CL_{TP,S,Org}^{SUB} = PS_{S,Org}^{SUB} \cdot \left(1 - \frac{C_{Org}^{I,SUB}}{C_{Org}^{V,SUB}} \right) \cdot \frac{Pe_{S,Org}^{SUB}}{e^{Pe_{S,Org}^{SUB}} - 1} + J_{S,Org} \cdot (1 - \sigma_S^{SUB}) \quad (24)$$

Table 2 State variables in the PBPK model

State variable	Unit	Definition
$C_{\text{Plasma}}^{\text{SUB}}$ ^a	M	Concentrations of “SUB” in central plasma
$C_{\text{Lymph}}^{\text{SUB}}$	M	Concentrations of “SUB” in the lymph nodes
$C_{\text{Org}}^{\text{V,SUB}}$	M	Concentrations of “SUB” in the vascular space of an organ
$C_{\text{Org}}^{\text{I,SUB}}$	M	Concentrations of “SUB” in the interstitial space of an organ
$C_{\text{Org}}^{\text{E,UB,SUB}}$	M	Concentrations of FcRn-unbound “SUB” concentrations in the endosomal space of an organ
$C_{\text{Org}}^{\text{E,B,SUB}}$	M	Concentrations of FcRn-bound “SUB” concentrations in the endosomal space of an organ
$A_{\text{BCLH}}^{\text{SUB}}$	mol	Amount of “SUB” in the lumped space containing Bowman’s capsule, proximal and distal tubules, and the loop of Henle (BCLH)
$FcRn_{\text{Org}}^{\text{IgG}}$	M	Free FcRn concentrations available for IgG Fc binding in endosomal space of an organ
$FcRn_{\text{Org}}^{\text{Alb}}$	M	Free FcRn concentrations available for albumin binding in endosomal space of an organ

^a“SUB” refers to the endogenous IgG (*enIgG*), endogenous albumin (*enAlb*), exogenous IgG (*exoIgG*), exogenous albumin (*exoAlb*), proteins with an albumin-binding domain (*Albud*), or the complex of the Albud protein bound to endogenous albumin (*AlbudAl*). As the “Methods” section explains, exogenously dosed FcRn non-binding molecules can be represented as *exoIgG*, and exogenously dosed albumin conjugates as *exoAlb*, with their MW and other properties adjusted as needed in the model variants

$Pe_{L,\text{Org}}^{\text{SUB}}$ and $Pe_{S,\text{Org}}^{\text{SUB}}$ are the Peclet numbers of a protein in large and small pores of an organ, defined as the ratio between convective transport and diffusive transport:

$$Pe_{L,\text{Org}}^{\text{SUB}} = \frac{J_{L,\text{Org}} \cdot (1 - \sigma_L^{\text{SUB}})}{PS_{L,\text{Org}}^{\text{SUB}}} \quad (25)$$

$$Pe_{S,\text{Org}}^{\text{SUB}} = \frac{J_{S,\text{Org}} \cdot (1 - \sigma_S^{\text{SUB}})}{PS_{S,\text{Org}}^{\text{SUB}}} \quad (26)$$

σ_L^{SUB} and σ_S^{SUB} are the vascular reflection coefficients for a protein in large and small pores [19]:

$$\sigma_L^{\text{SUB}} = 3.5 \times 10^{-5} \times MW_{\text{SUB}}^{0.717} \quad (27)$$

$$\sigma_S^{\text{SUB}} = 1 - 0.8489e^{-4 \times 10^{-5} \times MW_{\text{SUB}}} \quad (28)$$

Rates of fractional lymph flow through large and small pores ($J_{L,\text{Org}}$ and $J_{S,\text{Org}}$) are expressed as:

$$J_{L,\text{Org}} = J_{iso,\text{Org}} + \alpha_L \cdot J_{Org} = Xj \cdot J_{Org} + \alpha_L \cdot J_{Org} \quad (29)$$

$$J_{S,\text{Org}} = -J_{iso,\text{Org}} + \alpha_S \cdot J_{Org} = -Xj \cdot J_{Org} + \alpha_S \cdot J_{Org} \quad (30)$$

where, $J_{iso,\text{Org}}$ is expressed as a dependent variable of J_{Org} , with Xj being a constant determined by relative pore abundances [19]. $PS_{L,\text{Org}}^{\text{SUB}}$ and $PS_{S,\text{Org}}^{\text{SUB}}$ depend on the protein size, pore sizes, relative hydraulic conductance of large and small pores, and organ lymph flow rates [19]:

$$PS_{L,\text{Org}}^{\text{SUB}} = Xp \cdot \frac{1}{a_e^{\text{SUB}}} \cdot (0.3429e^{-1.2175 \times 10^{-4} \times MW_{\text{SUB}}} + 0.6571e^{-4.21 \times 10^{-6} \times MW_{\text{SUB}}}) \cdot \frac{\alpha_L}{r_L^2} \cdot J_{Org} \quad (31)$$

$$PS_{S,\text{Org}}^{\text{SUB}} = Xp \cdot \frac{1}{a_e^{\text{SUB}}} \cdot (0.2352e^{-8.295 \times 10^{-5} \times MW_{\text{SUB}}} + 0.7648e^{-5.3095 \times 10^{-4} \times MW_{\text{SUB}}}) \cdot \frac{\alpha_S}{r_S^2} \cdot J_{Org} \quad (32)$$

Model parameters

Detailed descriptions of the state variables and the parameters used in the model are provided in Tables 2 and 3, respectively. Physiological parameter values for mice, rats, monkeys, and humans were taken from [25], except that the central plasma volume (V_{Plasma}) is the total plasma volume subtracted by the sum of vascular volumes from all organs.

The lymph flow of each organ (J_{Org}) is set to 0.2% of the plasma flow into that organ (Q_{Org}), and the lymphatic reflection coefficient (σ'_{Org}) in all organs is all set to 0.2 [25]. The baseline endothelial pinocytosis rate (CL_{up}) and lysosomal degradation rate (K_{deg}) are set to 1.22 L/h/L and 15.3/h, respectively [20]. Given the almost complete tubular reabsorption of albumin, its fraction reabsorbed is set to 97% based on the literature reported range [33, 34]. In the current

Table 3 A glossary of parameters used in the two-pore PBPK model

Parameter	Unit	Definition	Value	Reference
Physiological parameters				
Q_{Org}, J_{Org}	L/h	Plasma flow to and lymph flow from an organ	-	[25]
L_{Lymph}	L/h	Clearance from lymph nodes	-	[25]
V_{Plasma}, V_{Lymph}	L	Volumes of the central plasma and lymph nodes	-	[25]
$V_{Org}^V, V_{Org}^{BC}, V_{Org}^E, V_{Org}^I, V_{Org}^C$	L	Volumes of the vascular, blood cell, endosomal, interstitial, and cellular compartments for an organ	-	[25]
σ_{Org}^I	-	Lymphatic reflection coefficient for an organ	0.2	[25]
$C_0^{enIgG}_{Plasma}$	M	Steady-state concentration of endogenous IgG in plasma	Mouse: 2.6×10^{-5} Rat: 3×10^{-5} Monkey: 6.6×10^{-5} Human: 6.6×10^{-5}	[17] [38]
$C_0^{enAlb}_{Plasma}$	M	Steady-state concentration of endogenous albumin in plasma	Mouse: 5.2×10^{-4} Rat: 6×10^{-4} Monkey: 6.4×10^{-4} Human: 6×10^{-4}	[39] [40] [41]
$K_{syn_{enIgG}}$	M/h	Synthesis rate of endogenous IgG in central plasma	Mouse: 4.3×10^{-6} Rat: 2.4×10^{-6} Monkey: 2.4×10^{-6} Human: 4.7×10^{-7} FHH patient: 4.9×10^{-7}	Calculated Supplementary Material
$K_{syn_{enAlb}}$	M/h	Synthesis rate of endogenous albumin in central plasma	Mouse: 2.8×10^{-4} Rat: 9.3×10^{-5} Monkey: 5.3×10^{-5} Human: 8.1×10^{-6} FHH patient: 1.3×10^{-5}	Calculated Supplementary Material
$K_{syn_{exIgG}}, K_{syn_{exoAlb}}, K_{syn_{Albud}}, K_{syn_{AlbudAl}}$	M/h	Synthesis rates of exoIgG, exoAlb, Albud, and AlbudAl in central plasma (redundant)	0	Fixed
Two-pore parameters				
MW_{SUB}	g/mol	Molecular weights of "SUB"	Vary case by case	Supplementary Table 1
a_e^{SUB}	nm	Hydrodynamic radius of "SUB"	Vary	Equation (20)
$J_{L,Org}, J_{S,Org}$	L/h	Lymph flow rates through large and small pores of an organ	Vary	Equations (29–30)
$J_{iso,Org}$	L/h	Isogravimetric lymph flow rate in an organ	$J_{iso,Org} = Xj \cdot J_{Org}$	Calculated
$PS_{L,Org}^{SUB}, PS_{S,Org}^{SUB}$	L/h	Permeability-surface area products of "SUB" through large and small pores of an organ	Vary	Equations (31–32)
$Pe_{L,Org}^{SUB}, Pe_{S,Org}^{SUB}$	-	Peclet numbers of "SUB" through large and small pores of an organ	Vary	Equations (25–26)
Xj	-	Proportionality constant that relates $J_{iso,Org}$ to J_{Org}	0.38	[19]
Xp	nm ³	A constant that relates $PS_{L,Org}^{SUB}$ and $PS_{S,Org}^{SUB}$ to J_{Org} and other parameters in Eqs. (31–32) expressed as $Xp = \frac{R \cdot T}{6\pi \cdot N} \times \frac{8}{\Delta P - \tilde{\sigma}_a \times \Delta \pi}$, where R is the gas constant (62.363 L • mmHg/K/mol), N is the Avogadro constant ($6.02 \times 10^{23}/mol$), T is body temperature (310 K), and $\Delta P - \tilde{\sigma}_a \times \Delta \pi$ is the startling force (1 mmHg)	13,197	[19]

Table 3 (continued)

Parameter	Unit	Definition	Value	Reference
r_L, r_S	nm	Radiuses of large and small pores	22.85, 4.44	[10]
α_L, α_S	-	Fractional hydraulic conductance of large and small pores	0.042, 0.958	[13]
$\sigma_L^{SUB}, \sigma_S^{SUB}$	-	Vascular reflection coefficients of “SUB” through large and small pores of an organ	Vary	Equations (27–28)
Renal handling parameters				
GFR	L/h	Glomerular filtration rate	Mouse: 0.0167 Rat: 0.154 Monkey: 1.116 Human: 7.2	[21] [42] [43] [44]
θ_{SUB}	-	Glomerular sieving coefficients of “SUB”	Vary	Equation (21) or Eq. (22)
$Frea_{enAlb}, Frea_{exoAlb}, Frea_{AlbuldAl}$	-	Fraction of filtered albumin and albumin-bound proteins reabsorbed	0.97	[34]
$Frea_{enIgG}, Frea_{exolgG}, Frea_{Albuld}$	-	Fraction of filtered <i>enIgG</i> , <i>exolgG</i> , and <i>Albuld</i> reabsorbed	0	Fixed
Q_{urine}	L/h	Urine flow rate	Mouse: 8.4×10^{-5} Rat: 4×10^{-4} Monkey: 1.56×10^{-2} Human: 5.8×10^{-2}	[18] [44]
V_{BCLH}	L	Volume of the lumped space containing Bowman's capsule, proximal and distal tubules, and the loop of Henle (BCLH)	9.5% of kidney volume	[16]
Endosomal processing parameters				
CL_{up}	L/h/L	Pinocytosis/exocytosis rate per unit endosomal volume in organs	1.22	[21]
CL_{up}^{Org}	L/h	Fluid phase pinocytosis rate of an organ	$CL_{up}^{Org} = CL_{up} \cdot V_{Org}^E$	Calculated
K_{deg}	1/h	First-order degradation rate constant of free antibody in the endosome	15.3	[21]
FR	-	Fraction of FcRn-bound proteins recycled to the vascular space	0.715	[45]
$FcRn_0^{IgG}$	M	Total FcRn concentrations for (endogenous and exogenous) IgG Fc binding in endosomal space of an organ	6.267×10^{-5}	Estimated
$FcRn_0^{Alb}$	M	Total FcRn concentrations for (endogenous and exogenous) albumin binding in endosomal space of an organ	$FcRn_0^{Alb} = 2FcRn_0^{IgG}$ Calculated	
$K_{on}^{FcRn,enAlb}, K_{on}^{FcRn,exoAlb}, K_{on}^{FcRn,AlbuldAl}$	1/M/h	Association rate constant for endogenous albumin and exogenous albumin derivatives (albumin from the same species by default) binding to FcRn	Mouse: 5.8×10^7 Rat: 2.7×10^7 Monkey: 1.9×10^7 Human: 2.7×10^7	[46]
$K_{off}^{FcRn,enAlb}, K_{off}^{FcRn,exoAlb}, K_{off}^{FcRn,AlbuldAl}$	1/h	Dissociation rate constant for endogenous albumin and exogenous albumin derivatives (albumin from the same species by default) binding to FcRn	Mouse: 43.9 Rat: 93.6 Monkey: 46.8 Human: 30.24	[46]
$K_{on}^{FcRn,enIgG}$	1/M/h	Association rate constant for endogenous IgG binding to FcRn	Mouse: 1×10^9 Rat: 1×10^9 Monkey: 1×10^9 Human: 5.6×10^8	[47] [17] [25]

Table 3 (continued)

Parameter	Unit	Definition	Value	Reference
$K_{off}^{FcRn,enIgG}$	1/h	Dissociation rate constant for endogenous IgG binding to FcRn	Mouse: 750 Rat: 280 Monkey: 68.2 Human: 23.9	[48] [47] [17] [25]
$K_{on}^{FcRn,exoIgG}$	1/M/h	Association rate constant for exogenously dosed IgG (human IgG1 by default) binding to FcRn	Mouse: 8.1×10^7 Rat: 8×10^8 Monkey: 1×10^9 Human: 5.6×10^8	[25] [25] [17] [25]
$K_{off}^{FcRn,exoIgG}$	1/h	Dissociation rate constant for exogenously dosed IgG (human IgG1 by default) binding to FcRn	Mouse: 6.55 Rat: 144 Monkey: 37.2 Human: 23.9	[25] [25] [17] [25]
$K_{on}^{FcRn,Albud}$	1/M/h	Association rate constant for Albud proteins binding to FcRn	0	Fixed
$K_{off}^{FcRn,Albud}$	1/h	Dissociation rate constant for Albud proteins binding to FcRn	1000	Fixed
Modality-specific parameters				
$K_{on}^{Alb,Albud}, K_{off}^{Alb,Albud}$	1/M/h, 1/h	Association and dissociation rate constants for Albud proteins binding to albumin	Vary case by case	Supplementary Table 1
$Spino_{enAlb}, Spino_{exoAlb}, Spino_{AlbudAl}$	-	Scale factor on the pinocytosis rate of albumin and albumin-bound proteins	Mouse: 0.579 Rat: 0.356 Monkey: 0.185 Human: 0.185	Estimated
$Spino_{enIgG}, Spino_{exoIgG}, Spino_{Albud}$	-	Scale factor on the pinocytosis rate of <i>enIgG</i> , <i>exoIgG</i> , and <i>Albud</i>	1	Fixed

model, it is assumed that the size of large pores and small pores (r_L of 22.85 nm and r_S of 4.4 nm), as well as the relative abundance of both pores (α_L of 0.042 and α_S of 0.958), are the same in all tissues [19]. Given the very wide range of experimentally determined endosomal total FcRn concentrations of 0.66–240 μM [35, 36], we estimated the total FcRn concentration available for endogenous and exogenous IgG binding ($FcRn_0^{IgG}$). $Spino_{SUB}$ values for most proteins in the study are set to 1, except for $Spino_{albumin}$, because albumin has an extremely low pI (~5–6) and hence strong negative charge that may lead to decreased pinocytotic uptake [37]. $Spino_{albumin}$ was estimated for individual species.

Considering the massive number of datasets utilized by the model, the concept of “model variants” is applied throughout. Each model variant contains alternative values of model parameters and/or initial conditions without creating additional models. Although only 6 categories of “*SUB*” is defined, all proteins can be described within the set “*SUB*”. For example, molecules with null FcRn interaction, such as F(ab)2, Fab, scFv, and nanobody, are characterized as “*exoIgG*” with $K_{on}^{FcRn,exoIgG}$ fixed to 0 and MW_{exoIgG} adjusted accordingly. Albumin conjugates are represented as “*exoAlb*” with MW_{exoAlb} defined as their actual MW. For Albud proteins, “ MW_{Albud} ”, “ $MW_{AlbudAl}$ ”,

“ $K_{on}^{Alb,Albud}$ ”, and “ $K_{off}^{Alb,Albud}$ ” need to be changed on case-by-case basis. Parameter values in each model variant for each modality are shown in Supplementary Table 1. Particularly, FHH patients are deficient in albumin and IgG because of reduced expression of FcRn. FcRn is a heterodimeric receptor composed of an MHC class I α -chain and $\beta 2$ -microglobulin ($\beta 2\text{m}$). It was found that the patients had a normal α -chain gene sequence but possessed a mutation in the signal sequence of $\beta 2\text{m}$. When the mutant $\beta 2\text{m}$ cDNA was transfected in cultured cells, the expression level of $\beta 2\text{m}$ is < 20% of that of normal $\beta 2\text{m}$ [49]. Accordingly, for FHH patients, the total endosomal FcRn concentration is set to only 20% of the normal level, and the plasma endogenous IgG and albumin concentrations (Table 2 and Supplementary Table 1) are also lower than healthy subjects based on the reported values [50].

There is generally a paucity of whole-body PK data of biologics in higher species. The only tissue distribution data for IgG and Albud (dAb) in humans and IgG in monkeys utilized ^{89}Zr -immuno-positron emission tomography (PET) imaging, which is known to confound PK of native proteins due to the residualizing nature of ^{89}Zr label. To avoid diverging from the focus of this manuscript, we did not further incorporate mechanisms of ^{89}Zr release, residualization, and enhanced tissue uptake in the model, as

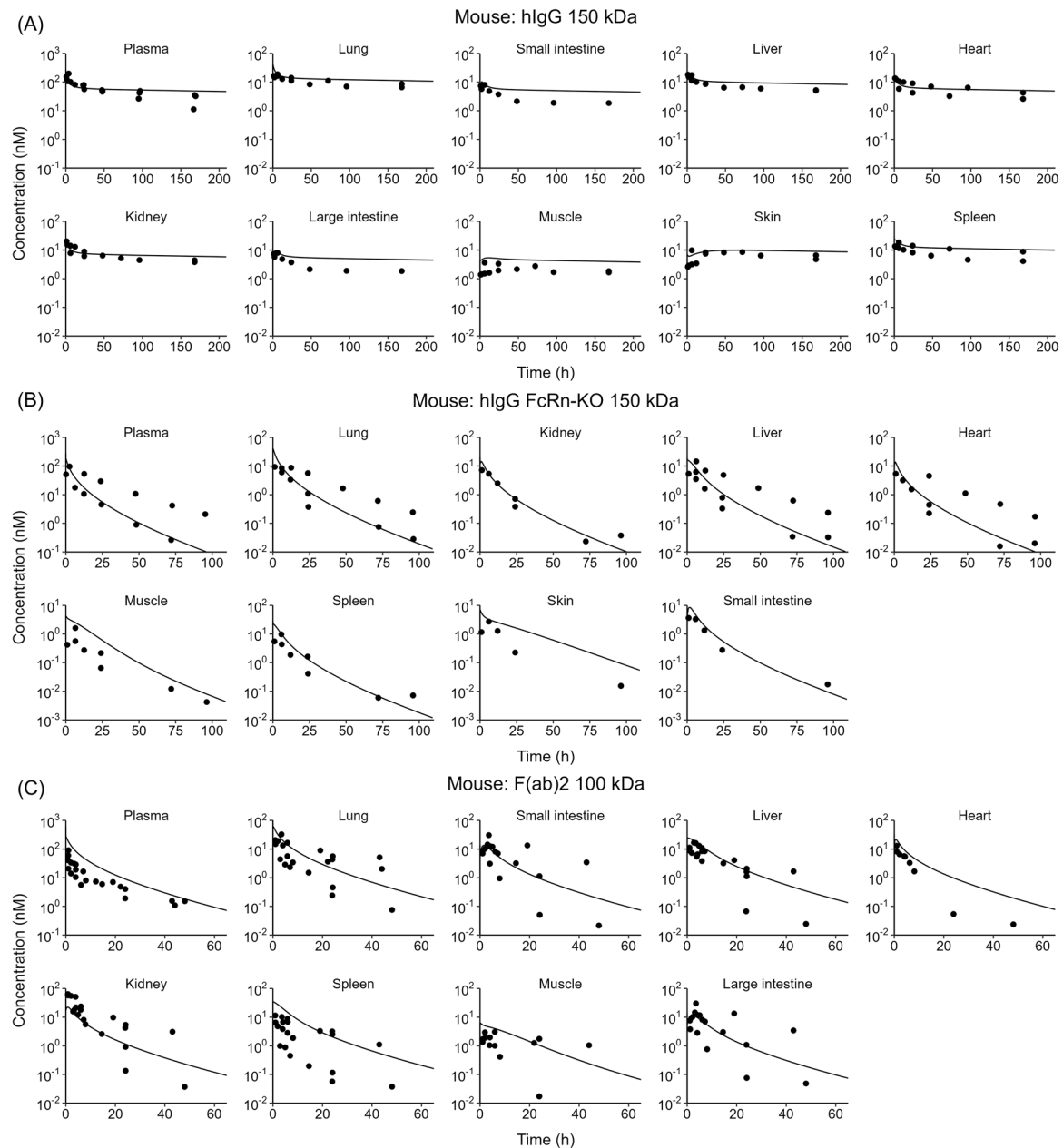
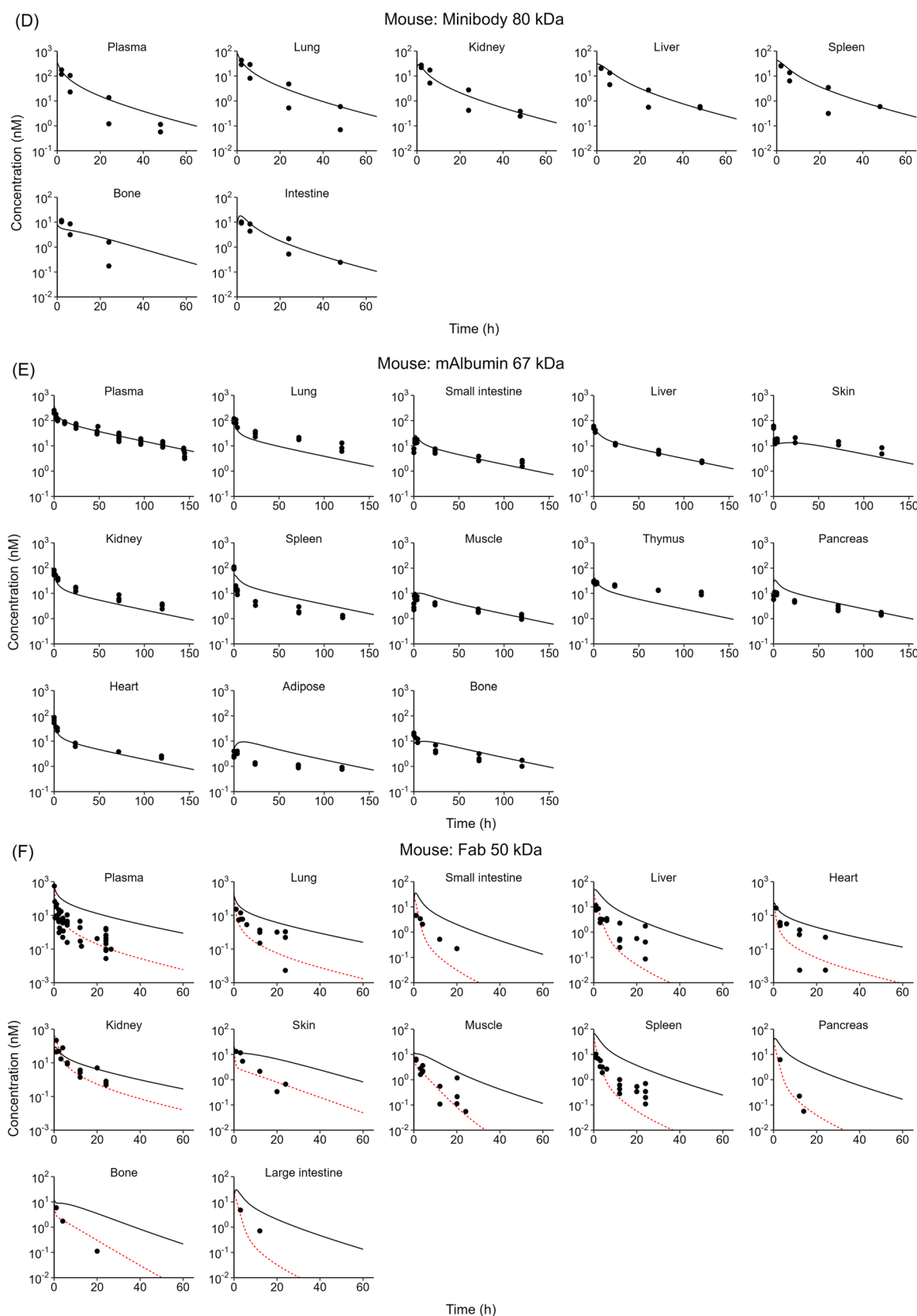


Fig. 2 The PBPK model predicted and observed plasma and tissue PK profiles of different-size proteins in mice. Solid symbols represent observed data, black lines are the default two-pore model predictions, and red lines are the model predictions for Fab using the sieving coefficient relationship described by Li and Shah. Data was pooled and normalized to 1 mg/kg dose level. The protein modalities

are: **A** human IgG (150 kDa), **B** human IgG (150 kDa) in FcRn KO mice, **C** F(ab)2 (100 kDa), **D** minibody (80 kDa), **E** mouse albumin (67 kDa), **F** Fab (50 kDa), **G** scFv (27 kDa), **H** dAb2 (23.5 kDa), **I** Albuld (dAb2) (23.5 kDa), **J** nanobody (13 kDa), and **I** other modalities including scFv-IgAb (205 kDa), scFv-Fc (105 kDa), TandAb (110 kDa), and nanobody-PAS600 (60 kDa)

**Fig. 2** (continued)

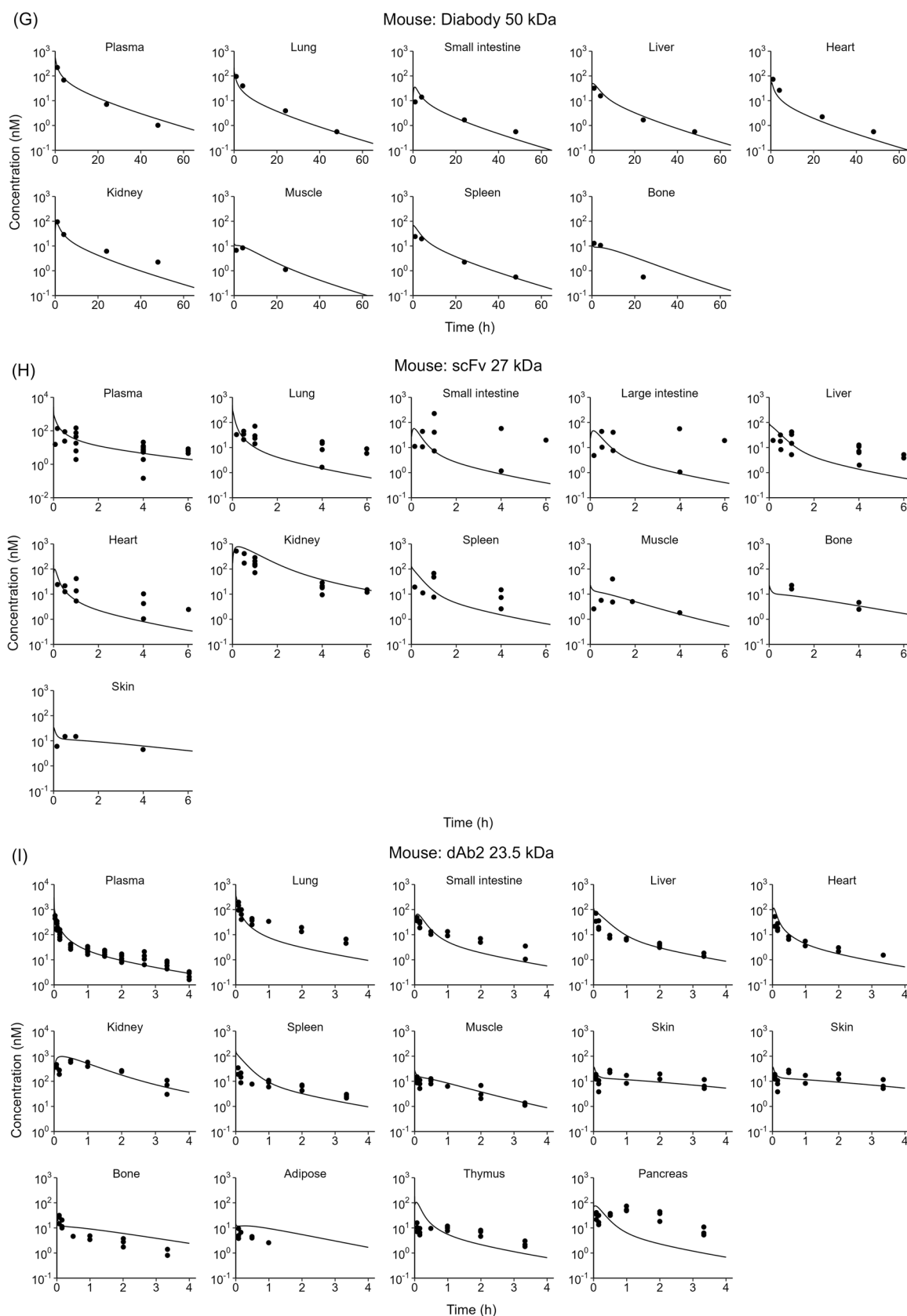
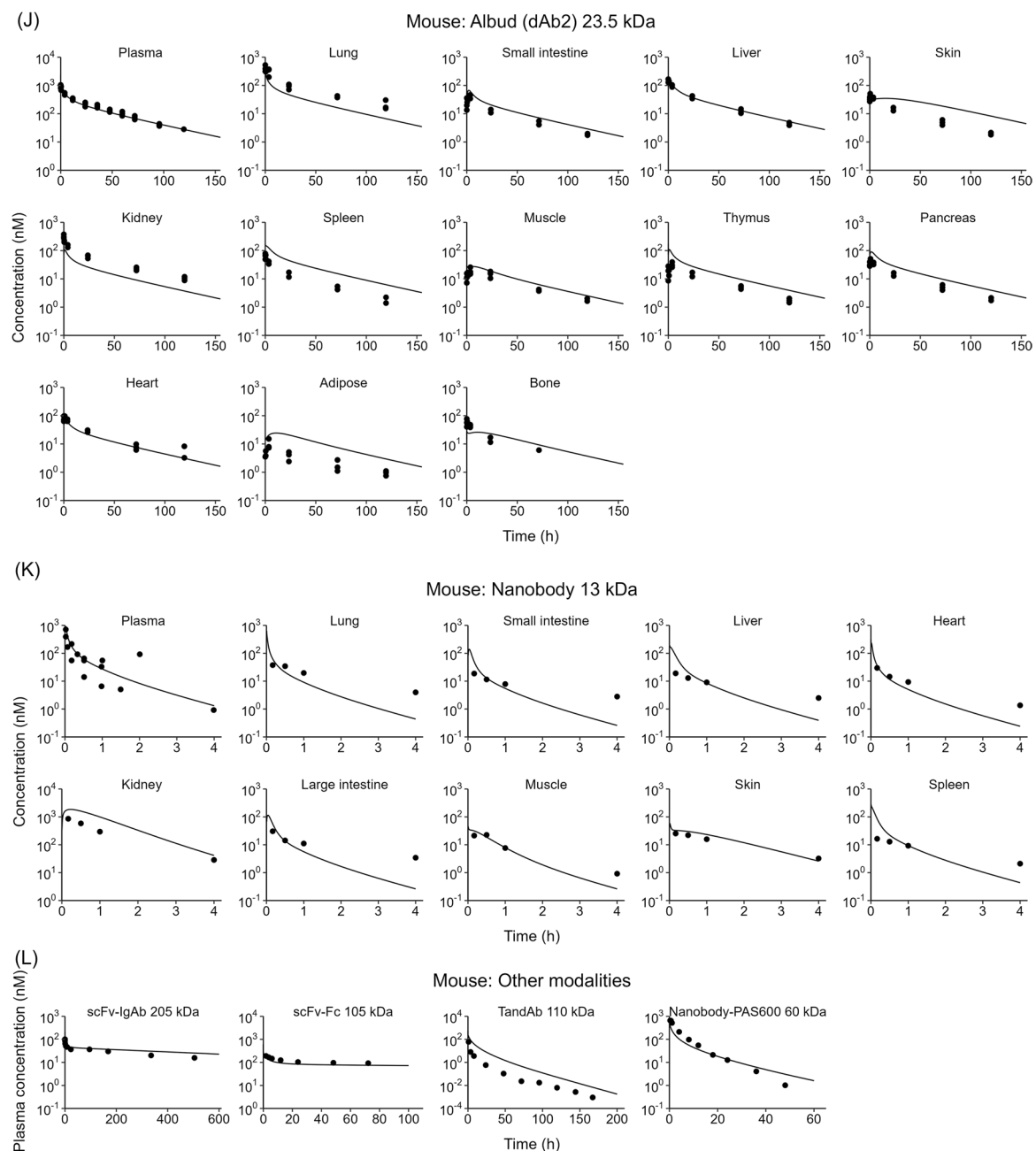


Fig. 2 (continued)

**Fig. 2** (continued)

done elsewhere by others and us [18, 51]. Instead, we utilized previously summarized tissue-specific scale factors, which, when multiplied by the ^{89}Zr radioactivity, yields the “true” concentration of the antibody as if the antibody is administered as the native form [51]. Specifically, we

divided the two-pore model outputs by these scale factors (0.95 for lung, 0.64 for liver, 0.95 for pancreas, 0.68 for spleen, and 0.91 for muscle and heart, 0.47 for kidney, 0.92 for adipose) to represent ^{89}Zr concentrations in comparison with observed data of ^{89}Zr labeled IgG [51].

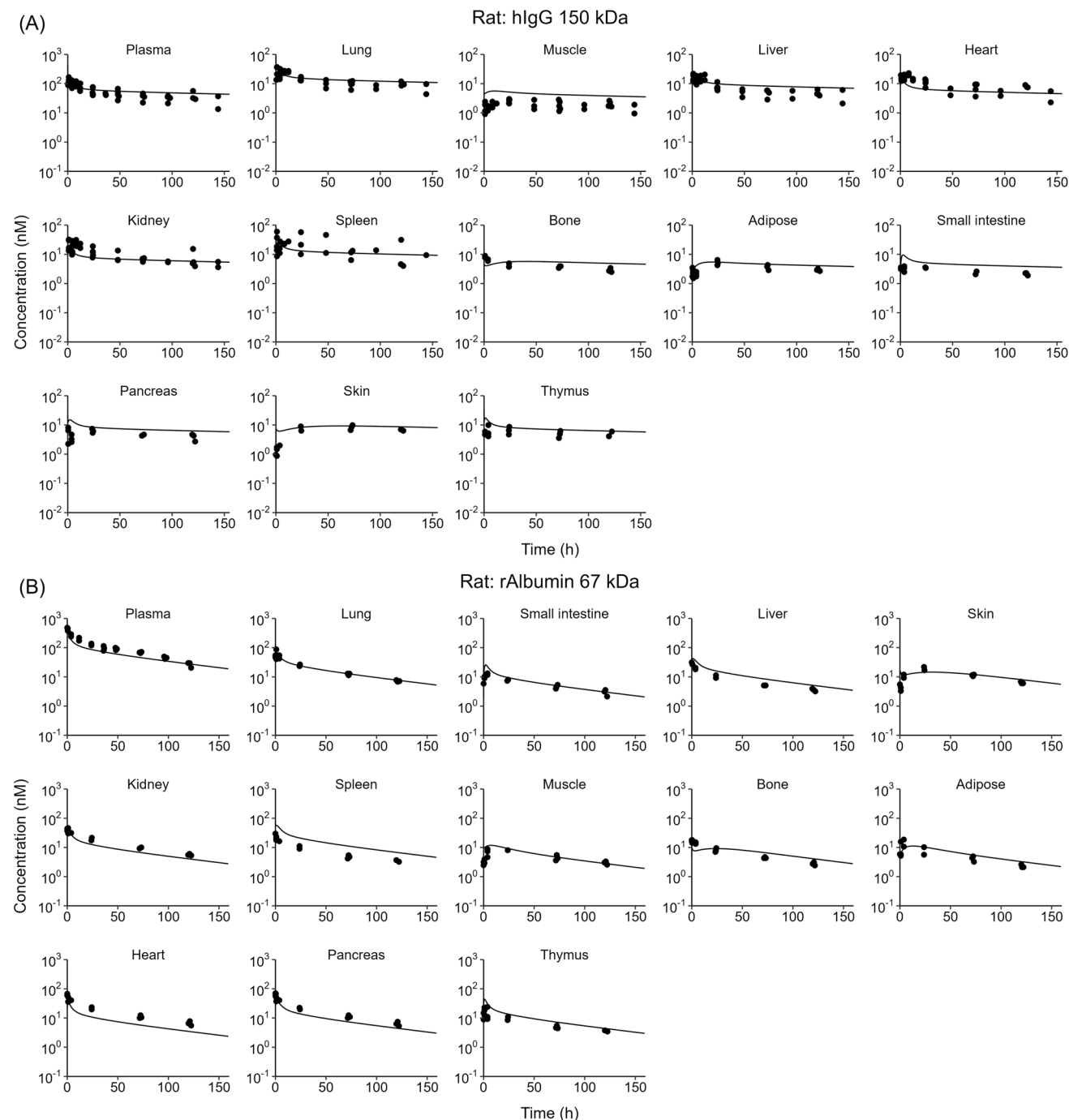
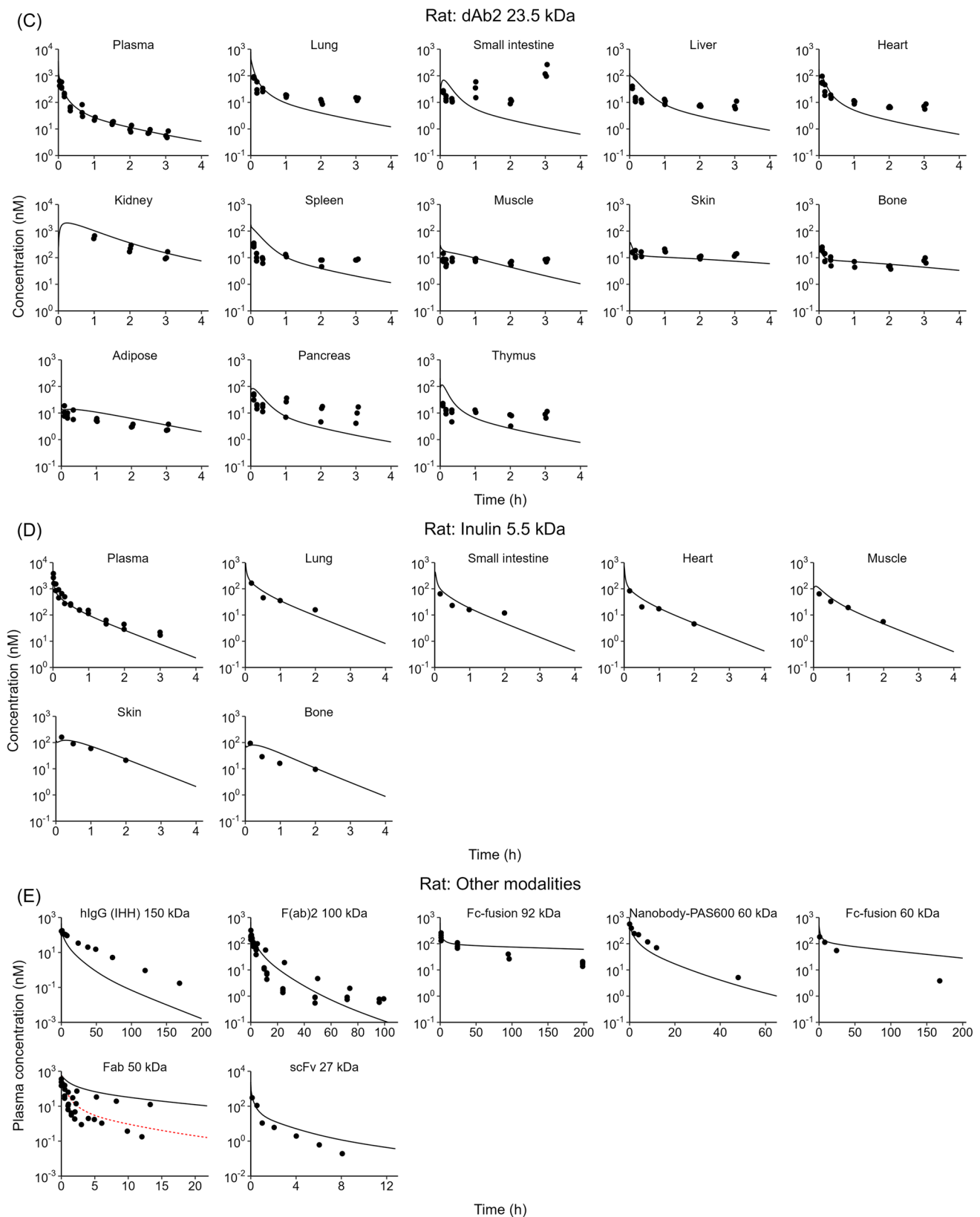


Fig. 3 The PBPK model predicted and observed plasma and tissue PK profiles of different-size proteins in rats. Solid symbols represent observed data, black lines are the default two-pore model predictions, and the red line is model predictions for Fab plasma PK using the sieving coefficient relationship described by Li and Shah. Data was pooled and normalized to 1 mg/kg dose level. The protein

modalities are: **A** human IgG (150 kDa), **B** rat albumin (67 kDa), **C** dAb2 (23.5 kDa), **D** inulin (5.5 kDa), and **E** other modalities including FcRn nonbinding human IgG (150 kDa), F(ab)2 (100 kDa), Fc-fusions of 92 kDa and 60 kDa, nanobody-PAS600 (60 kDa), Fab (50 kDa), and scFv (27 kDa)

For the Albul (dAb) dataset [18], we excluded bone and kidney PK, due to the fact that dissociated ^{89}Zr is largely taken up into the bone and can be freely filtered into the renal tubule [51], which is not specified in the current

two-pore model. Although the influence of free ^{89}Zr on Albul (dAb) signal is unclear compared to IgG, we expect ^{89}Zr labeling to also cause less than twofold changes in the detected concentrations relative to native Albul (dAb),

**Fig. 3** (continued)

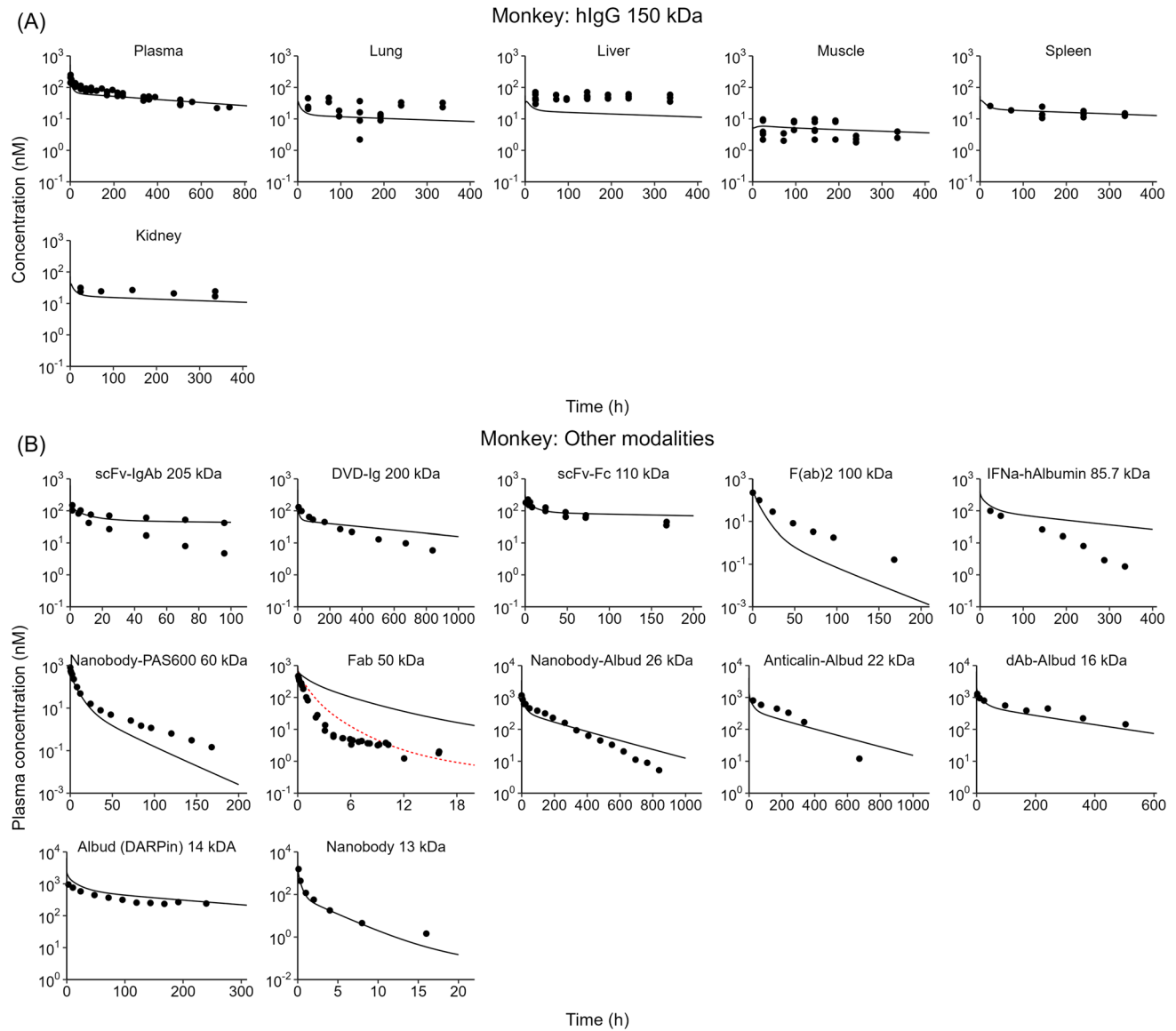


Fig. 4 The PBPK model predicted and observed plasma PK profiles of different-size proteins in monkeys. Solid symbols represent observed data, black lines are the default two-pore model predictions, and the red line is model predictions for Fab plasma PK using the sieving coefficient relationship described by Li and Shah. Data was pooled and normalized to 1 mg/kg dose level. The protein modalities include A human IgG (150 kDa), B scFv-IgAb (205 kDa), DVD-Ig (200 kDa), scFv-Fc (110 kDa), F(ab)2 (100 kDa), IFN α -human albumin conjugate (85.7 kDa), nanobody-PAS600 (60 kDa), Fab (50 kDa), nanobody-Albud (26 kDa), anticalin-Albud (22 kDa), dAb-Albud (16 kDa), Albud (DARPin) (14 kDa), and nanobody (13 kDa)

ties include A human IgG (150 kDa), B scFv-IgAb (205 kDa), DVD-Ig (200 kDa), scFv-Fc (110 kDa), F(ab)2 (100 kDa), IFN α -human albumin conjugate (85.7 kDa), nanobody-PAS600 (60 kDa), Fab (50 kDa), nanobody-Albud (26 kDa), anticalin-Albud (22 kDa), dAb-Albud (16 kDa), Albud (DARPin) (14 kDa), and nanobody (13 kDa)

given similarly long half-lives of Albud (dAb) and IgG. Therefore, model outputs were directly compared with the ^{89}Zr labeled Albud (dAb) PK data in humans without further modifications.

Model estimation and simulation

Model optimization was performed in 3 steps. First, the model was confirmed to be able to appropriately describe whole-body PK of different-size proteins lacking FcRn

binding across the four species. Subsequently, IgG PK data from all species were simultaneously fitted to enable estimation of a universal $FcRn_0^{IgG}$. Lastly, albumin PK data were fitted to estimate species-specific $Spino_{albumin}$. Of note, due to the lack of albumin PK studies conducted in monkeys, the data of albumin-related modalities including an albumin conjugate and Albud proteins from monkeys were pooled with albumin data from humans to estimate a single $Spino_{albumin, primate}$. Model fitting was performed in R using the *Ubiquity* package (v2.0.0) [52], to obtain

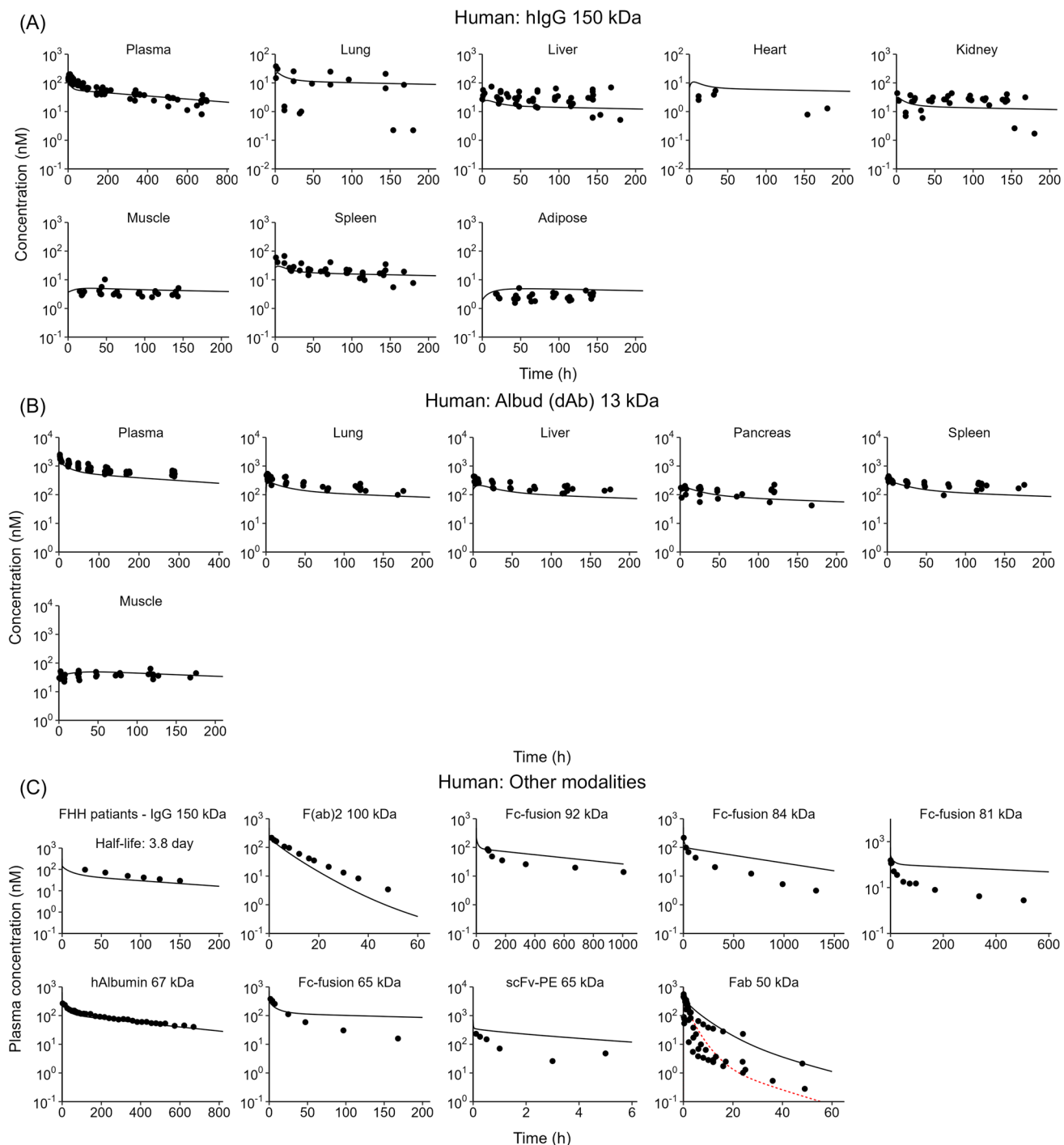


Fig. 5 The PBPK model predicted and observed plasma and tissue PK profiles of different-size proteins in humans. Solid symbols represent observed data, black lines are the default two-pore model predictions, and the red line is model predictions for Fab plasma PK using the sieving coefficient relationship described by Li and Shah. Data

the maximum likelihood estimates of parameters with a combined error variance model. Each model simulation involves two stages: (1) the system stabilization phase that runs from -500 h to 0 h to allow endogenous IgG and

was pooled and normalized to 1 mg/kg dose level. The protein modalities are: **A** human IgG (150 kDa), **B** Albud (dAb) (13 kDa), and **C** other modalities including human IgG (150 kDa) in FHH patients, F(ab)2 (100 kDa), Fc-fusion proteins of different MW (92, 84, 81, and 65 kDa), human albumin (67 kDa), scFv-PE, and Fab (50 kDa)

albumin to reach steady states in every compartment; (2) the post-dosing phase following intravenous administration of proteins at time 0. The concept of “mathematical sets” employed in the *Ubiquity* package makes it simple

to assemble different organs, protein modalities, and species, which help avoids repetitive, error-prone coding and ensuring consistency of the model structure in all scenarios (<https://r.ubiquity.tools/articles/Language.html>). Mass balance of different-size proteins in all species was confirmed to be 100%.

To evaluate model performance, we calculated percent prediction error (%PE) of area under the curve (AUC) of PK data (time 0 to time of the last observation) for each modality in each species using the following unbiased equation [53]:

$$\%PE = \begin{cases} \left(1 - \frac{AUC_{obs}}{AUC_{pred}}\right) \times 100, & AUC_{pred} < AUC_{obs} \\ \left(\frac{AUC_{pred}}{AUC_{obs}} - 1\right) \times 100, & AUC_{pred} \geq AUC_{obs} \end{cases} \quad (33)$$

Two-fold overprediction and underprediction correspond to %PE of 100% and -100%, respectively.

Pathway analysis was also conducted to analyze contribution of renal filtration and endosomal catabolism in eliminating different-size proteins, as well as their transcapillary mass transport attributed to diffusion/convection through large and small pores and Fc-mediated

transcytosis (associated equations are presented in the Supplementary Material).

Results

PBPK modeling of different-size proteins without FcRn binding

The PBPK model was used to first characterize all modalities with no FcRn binding capabilities to eliminate the confounding impact of FcRn-mediated salvage. PK data of the majority of these proteins, ranging in size from 5.5 kDa to 150 kDa, in all 4 species were characterized reasonably well (Figs. 2B, C, D, G, H, I, K, L, 3C, D, E, 4B, and 5C). Notably, consistent overpredictions of Fab PK were observed in all species (Figs. 2F, 3E, 4B, and 5C). However, this should not be simply interpreted as model misspecification for that size of proteins, since model predictions for whole-body PK well matched the observed data for diabody, which has the same MW as a Fab (i.e., 50 kDa) (Fig. 2G). Further exploration revealed that usage of the alternative size-dependent sieving coefficient relationship derived by Li and Shah can better describe Fab PK (Figs. 2F, 3E, 4B, and 5C). This is a typical example where physicochemical properties other than size, such as molecular charge and conformation, may significantly impact protein PK via altered renal filtration or other disposition processes. These mechanisms may also explain model deviations seen for FcRn-nonbinding IgG in rats (Fig. 3E), F(ab)2 in monkeys (Fig. 4B), and scFv-PE in humans (Fig. 5C).

Table 4 Parameter estimates and associated uncertainties

Parameter	Unit	Estimate	CV%
<i>FcRn_0IgG</i>	M	6.267×10^{-5}	2.10
<i>Spino_{albumin,mouse}</i>	-	0.579	2.17
<i>Spino_{albumin,rat}</i>	-	0.356	1.92
<i>Spino_{albumin,primate}</i>	-	0.185	2.19

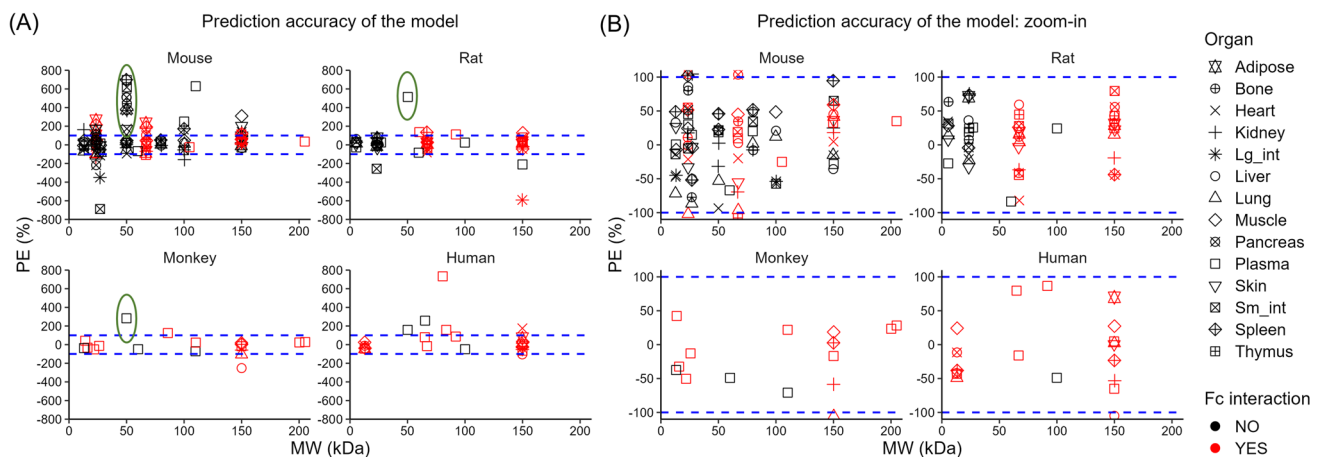


Fig. 6 Overview of the PK prediction accuracy of the default two-pore model across a wide range of MW. **A** PE% of AUC_{0-t} of different-size proteins versus protein MW in mice, rats, monkeys, and humans. **B** a zoom-in image of (A) for data whose prediction error was within two-fold. Data from different organs are indicated by vari-

ous shapes. Proteins with and without FcRn binding are colored red and black, respectively. Blue dotted lines indicate $\pm 100\%$ of PE%. Data points within the green circles represent Fab PK predicted by the default two-pore model, which are better characterized using the sieving coefficient relationship by Li and Shah

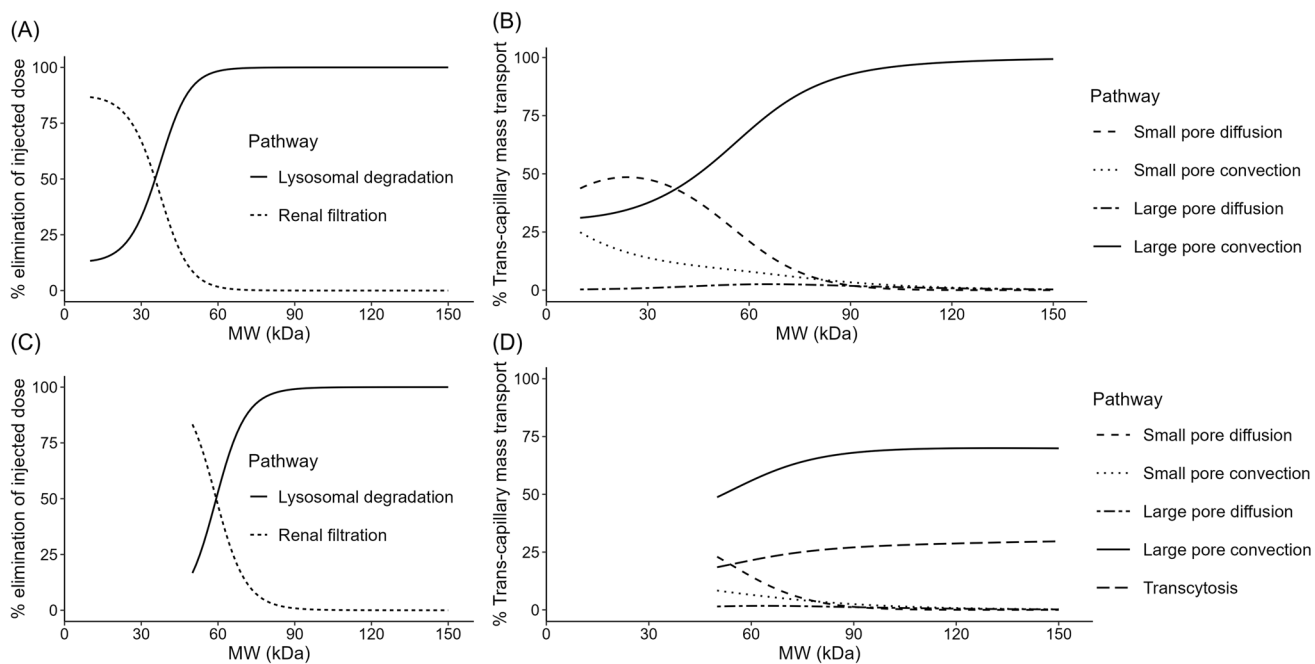


Fig. 7 Pathway analysis of the two-pore PBPK model. Percentage contribution of renal filtration and lysosomal degradation towards total elimination of different-size proteins in the absence of tubular reabsorption without FcRn binding (**A**) or with IgG1 Fc (**C**) in

humans. Percentage of transcapillary transport through large and small pores via diffusion and convection and FcRn-mediated transcytosis for molecules without FcRn binding (**B**) and with IgG1 Fc (**D**) in humans

PBPK modeling of FcRn-binding IgG and Fc-fusion proteins

After confirming the accuracy of the model in predicting PK of FcRn non-binding molecules, we proceeded to characterize FcRn-Fc interactions. Given the nearly 400-fold range of literature reported FcRn concentrations in endosomes (0.66–240 μM), we estimated this parameter, $FcRn_0^{IgG}$, using IgG PK data in all species. $FcRn_0^{IgG}$ was estimated to be 63 μM (CV% of 2.1%). Antibody PK across all species was generally captured well (Figs. 2A, 3A, 4A, and 5A), yet significant underpredictions in the liver were observed for monkeys, perhaps because the influence of ^{89}Zr labelling on antibody uptake into the liver is not incorporated within the model. Meanwhile, PK of other proteins containing Fc were also well characterized in mice (Fig. 2L), rats (Fig. 3E), and monkeys (Fig. 4B), although PK data of Fc-fusion proteins (MW of 92, 84, 81, and 65 kDa) was modestly overpredicted in humans (Fig. 5C). Simulated IgG PK in FHH patients is in line with observations, with a predicted half-life of about 3.8 days corresponding to the reported half-life of 3.3-days [50].

PBPK modeling of albumin, albumin conjugate, and Albuld molecules

Albumin-related data were separated out when estimating $FcRn_0^{IgG}$ above, because initially we noticed substantial

underpredictions of albumin PK, to greater extents in higher species (data not shown). This brought to our attention the unusually low pI values of albumin ($\text{pI} \sim 5\text{--}6$) compared to mostly positively charged therapeutic proteins incorporated in this dataset. Such negative charge not only leads to almost 100-fold reduction in its glomerular sieving coefficient compared to positively charged molecules (Supplementary Figure 3), but also is expected to decrease nonspecific pinocytosis due to electrostatic repulsion from cell membrane [37]. Therefore, we estimated the modification factors on pinocytosis of albumin, $Spino_{\text{albumin}}$, for mice, rats, and primates (monkeys and humans) to be 0.579, 0.356, and 0.185, respectively (Table 4). Consequently, whole-body PK of albumin (Figs. 2E, 3B, and 5C) and a diverse panel of Albuld molecules (Figs. 2J, 4B, and 5B) and an albumin conjugate (Fig. 4B) were all described well by the model.

Overall evaluation of the model performance and properties

The accuracy of model predictions was evaluated by comparing the simulated AUC values with the observed average AUC in each scenario, using the %PE metric. To have a high-level understanding of whether the performance of the two-pore model in predicting PK is biased by: (1) protein size, (2) metrics such as plasma versus different tissues, (3) the presence of FcRn binding, and (4) animal species, we

assessed %PE stratified by these factors (Fig. 6). Except for Fab molecules that cannot be captured using the default two-pore model (Fig. 6A), the majority of the protein modalities, regardless of their MW, FcRn interactions, and in which matrix they were measured, were adequately predicted by the model with less than two-fold errors in AUC (Fig. 6B). Although a few outliers still exist (i.e., $| \%PE | > 100\%$), no systematic trend was noticed.

We further evaluated the importance of different elimination pathways for different-size proteins (Fig. 7A and C). It is evident that in the absence of FcRn binding, proteins with $MW > 60$ kDa are eliminated exclusively via lysosomal catabolism, whereas proteins with $MW < 20$ kDa are mostly cleared by renal filtration. When the MW of a protein is ~ 36 kDa, catabolism and renal elimination are equally important (Fig. 7A). Of note, such conclusions were drawn under the default two-pore model framework. For proteins that are better described by the sieving coefficient relationship by Li and Shah, renal elimination may be more significant than depicted in Fig. 7A. Moreover, the contribution profile shows a right-shift in the presence of FcRn binding (Fig. 7C), as lysosomal degradation becomes diminished due to FcRn-mediated salvage. On the other hand, contribution of diffusion and convection via large and small pores and Fc-mediated transcytosis towards transcapillary transport was examined (Fig. 7B and D). It was found that without FcRn binding, diffusion via small pores and convection through large pores are two leading transport mechanisms across the wide range of MW. Proteins larger than 90 kDa extravasate almost entirely from large pores via convection, whereas proteins smaller than 30 kDa transport primarily through small pores via diffusion (Fig. 7B). However, for molecules with a $MW > 90$ kDa and with FcRn binding, FcRn-mediated transcytosis and large pore convection can contribute to roughly 30% and 70% of transcapillary transport, respectively (Fig. 7D).

Discussion

The potential of the two-pore theory in describing tissue distribution of different-size proteins has been appreciated for decades [10, 11]. A few pivotal works have facilitated its application in PBPK models for biologics [12–17, 19]. However, the cross-modality, cross-species capability of two-pore PBPK modeling still remains uncertain, as published models either lack adequately diverse protein modalities for validation or did not test extrapolation across species.

To address this gap, in the present study we have developed and optimized a two-pore PBPK model for different-size proteins in preclinical animals and humans. The model was constructed largely based on the two-pore theory by Rippe and Haraldsson [10, 11] and the derivations by Sepp

et al. [16] and Li and Shah [19]. The unified model can describe whole-body PK of different-size proteins owing to a series of MW-dependent parameters, including the permeability-surface area product (PS), the vascular reflection coefficient (σ), Peclet number (Pe), and the sieving coefficient (θ). Characterization of diverse modalities is also enabled by the idea of “model variants”, where the 6 substances specified in the model (*enIgG*, *enAlb*, *exoIgG*, *exoAlb*, *Albuld*, *AlbuldAI*) suffice to reflect the majority of existing protein therapeutics. The model was first validated for its ability to a priori predict whole-body PK of different-size proteins lacking FcRn binding in all 4 species. Subsequently, IgG PK data across species was utilized to obtain the estimate of endosomal total FcRn concentration ($FcRn_0^{IgG}$). Last, modification factors on pinocytosis of albumin were estimated in all the species.

The finalized model was able to describe PK of a diverse array of endogenous and exogenous proteins in mice, rats, monkeys, and humans reasonably well. These modalities have constituted the most densely sampled MW range ever tested in two-pore models, including inulin (5.5 kDa, a polysaccharide rather than a protein), nanobody (13 kDa), Albuld proteins (13, 14, 16, 22, 23.5, and 26 kDa), dAb2 (23.5 kDa), scFv (27 kDa), diabody (50 kDa), Fab (50 kDa), albumin (67 kDa), minibody (80 kDa), albumin conjugate (85.7 kDa), Fc-fusion proteins (60, 65, 81, 84, 92, 105, 110, 200, and 205 kDa), F(ab)2 (100 kDa), IgG (150 kDa). Among them, albumin/albumin conjugate/albumin-bound Albuld and IgG/Fc-fusion proteins are allowed to bind to 2 independent sites of FcRn and compete with endogenous counterparts for FcRn binding. AUC values of plasma and tissue PK data for most protein modalities in the 4 species were predicted within twofold error ($| \%PE | < 100$), irrespective of their MW and FcRn binding.

After model optimization, pathway analysis was conducted to obtain mechanistic insights into size-dependent renal filtration and extravasation processes. Consistent with the consensus of the cutoff MW for glomerular filtration being 60–70 kDa [54, 55], we found that proteins with MW larger than 60 kDa are cleared almost completely via lysosomal degradation. For proteins smaller than 60 kDa, the contribution of renal filtration towards total elimination is greater as MW decreases (~85% for 10-kDa proteins). We also examined the contribution of diffusion and convection via both pores and transcytosis towards protein extravasation. It was found that proteins larger than 90 kDa extravasate exclusively via convective transport through large pores and FcRn-mediated transcytosis (if with the FcRn binding capability), supporting the one-pore convection formalism applied in many mAb PBPK models [25, 45]. For proteins smaller than 30 kDa, small pore diffusion followed by large pore convection are the leading extravasation mechanisms (contribution ~80% in total).

Characterization of FcRn interactions

The binding between albumin and FcRn, and between IgG and FcRn, follow distinct stoichiometries of 1:1 and 1:2, respectively [28, 29]. Sepp et al. accounted for the stoichiometric difference by assuming that recycling rate of IgG is half that of albumin [17], but we argue that the number of FcRn bound to the molecules should not impact the proportion of molecules recycled per unit time. Moreover, because IgG and albumin do not compete for the same binding site on FcRn, the model theoretically allows albumin-bound FcRn to also bind IgG. Then the FcRn, when concurrently bound to IgG and albumin, should have one constant recycling rate, rather than two rates. Therefore, we set the initial concentration of FcRn binding sites for albumin to twice that for IgG ($FcRn_0^{Alb} = 2FcRn_0^{IgG}$) while keeping the FcRn recycling rate invariant. This implies that $FcRn_0^{Alb}$ represents the actual endosomal FcRn concentration.

The total FcRn concentration for IgG binding, $FcRn_0^{IgG}$, was estimated to be 63 μM, which is higher than the values used in several other versions of PBPK models incorporating endogenous IgG, such as 9 μM in [17], 33 μM in [27, 56], 40 μM in [57]. This discrepancy originates from different model settings. In Sepp et al.'s two-pore model, the endosomal uptake rate (k_{up}) is close to ours (k_{up} of 0.9/h vs. CL_{up} of 1.22 L/h/L), but they allowed the endosomal recycling rate (k_{rec}) for IgG to be as high as 11.7/h [17]. In contrast, we have set the recycling rate to match the uptake rate, based on our perception that the volumes for pinocytosis and exocytosis per unit time should be equal. The markedly rapid recycling in their model can thus compensate for the low FcRn concentration of 9 μM. On the other hand, FcRn concentration of 33 μM was used in a series of antibody one-pore and two-pore models that account for endogenous IgG [27, 56]. In these models, catenary endosomal sub-compartments were used to describe endosomal processing of IgG as pH gradually changes, with endosomal volumes, pinocytosis rate, and endosomal transit time interdependent [58]. Nevertheless, translating their CL_{up}^{Org} values in the context of our model setting (assuming endosomal volumes to be 0.5% of tissue volumes) reveals considerably lower pinocytosis rates per unit endosomal volume (CL_{up} of 0.03 L/h/L [27] or 0.4 L/h/L [56] compared to our CL_{up} of 1.22 L/h/L). Consequently, lower nonspecific uptake necessitates less endosomal FcRn in these models. Not surprisingly, when reproducing such antibody two-pore catenary sub-compartment PBPK model [27] and further simulating different-size protein PK, we observed consistent overpredictions of smaller-size protein PK (data not shown), due to the excessively slow pinocytosis for molecules without FcRn interaction. Slow pinocytosis (k_{up} of 0.03/h) coupled with much faster recycling (k_{rec} of 0.6/h)

also explains why a lower concentration of FcRn (40 μM) is needed in another two-pore minimal PBPK model [57].

Despite the discrepancies between the previously reported models and the present model, the estimated $FcRn_0^{IgG}$ of 63 μM and $FcRn_0^{Alb}$ of 126 μM fall within the wide range of experimentally measured total FcRn concentrations. In one study employing immune-affinity liquid chromatography mass spectrometry, hFcRn concentrations in homozygous Tg32 transgenic mice were found to range from 8 pmol/g tissue for brain and 111 pmol/g tissue for lymph nodes [59], corresponding to endosomal concentrations of 1.6–22 μM assuming the endosomal volume to be 0.5% of the tissue volume. This method has also revealed FcRn tissue expression in humans to range from 3.3 pmol/g tissue for heart and 231 pmol/g tissue for spleen (i.e., 0.66–46 μM in the endosome) [35]. Additionally, using a quantitative Western blot method, Li and Balthasar determined the tissue FcRn concentrations to range from 18 nM in muscle and 802 nM in kidney [60], which translates to endosomal concentrations of 3.6–160 μM. A similar method has been applied to obtain the FcRn concentration in HepG2 cells as 270 ng/mg total protein [36], which can be converted to the endosomal concentration of 240 μM (based on 170 pg protein/HepG2 cell [61] and 0.85 pL of HepG2 cell volume [62]).

Currently, different assumptions regarding FcRn concentrations exist in different PBPK models. While the present two-pore model and several other models keep the total FcRn concentration the same across species, it was determined that the total FcRn concentration in humans was higher than that in mice and monkeys in the PK-Sim model [15]. In fact, the conclusion that FcRn concentration in humans is higher than that in other species would have been drawn, if we had allowed FcRn concentrations to be different among species in model fitting (data not shown). Meanwhile, maintaining species-invariant total FcRn concentrations will lead to decreased free FcRn available for exogenous IgG binding in higher species, as shown in Supplementary Figure 2, which is also different from the assumption made in our one-pore platform antibody PBPK model that the free FcRn concentrations (49.8 μM) are the same across species [25]. A holistic study that investigates FcRn concentrations in mice (wildtype vs. human FcRn transgenic), rats, monkeys, and humans using the same methodology would be helpful to determine what assumption regarding FcRn concentrations across species should be adopted.

We also wanted to point out the numerical interdependency between the FcRn concentration ($FcRn_0^{IgG}$) and the endosomal protein degradation rate (K_{deg}) in PBPK models, despite the physiological independence of these two parameters. We noted that K_{deg} is not influential in the PK of proteins lacking the FcRn binding capability (data not shown), because these proteins' disposition is primarily determined by the nonspecific pinocytosis (CL_{up}) that serves

as a dead-end elimination pathway. K_{deg} only becomes a sensitive parameter in the presence of FcRn-mediated salvage due to the competition between catabolism and recycling. Recognizing the uncertainty in the literature regarding values of K_{deg} and $FcRn_0^{IgG}$ (K_{deg} reported to be 5.3/h [57], 12.3/h in [15], 15.3/h in [21], 20.35/h in [53], and 152.8/h in [17]; $FcRn_0^{IgG}$ reported to be 0.66–240 μM as discussed above), we initially tried to estimate both parameters simultaneously. However, when conducting the robustness analysis post-estimation, we found that quite a few, if not infinite, pairs of values for K_{deg} and $FcRn_0^{IgG}$ within the literature reported ranges yielded equally satisfactory fitting results with the same minimal Akaike Information Criterion (AIC) value. These optimal solutions exhibited a positive correlation between K_{deg} and $FcRn_0^{IgG}$, which appears more of an identifiability issue than inability to find the global minimum. Therefore, here we just kept the value of K_{deg} the same as reported by us previously (15.3/h) instead of recalibrating it and estimated only $FcRn_0^{IgG}$, but it is worth noting that these two values can be updated in the future once consensus measurements are obtained.

Interestingly, overpredictions of PK data of Fc-fusions in humans were consistently observed (Fig. 5C). Although fusing proteins to the IgG Fc is a well-established strategy to prolong their persistence in circulation, it is quite common that Fc-fusion proteins still exhibited a shorter half-life than human IgG1 (<5 days vs. 21 days), albeit with a MW similar to that of IgG [63, 64]. It has been observed that several Fc-fusion proteins showed 4–sixfold lower affinity to FcRn than mAbs, which is attributed to the conformational change of the CH2-CH3 interface (i.e., FcRn binding region) induced by the fusion partner [65, 66]. Accordingly, the two-pore model can characterize PK of Fc-fusion proteins more accurately when the FcRn binding affinity is set modestly lower (data not shown).

Influence of molecular attributes other than MW

We compared two different MW-dependent glomerular sieving coefficient relationships in the model. While the equation generated by Sepp et al. was adequate for most molecules, we observed that Fab PK was consistently overpredicted and better characterized using the equation fitted by Li and Shah. However, this does not mean that the latter only works for Fab, nor does it suggest that physicochemical properties of Fab must be distinct from others. Protein PK is particularly sensitive to renal filtration when $MW < 60$ –70 kDa. Above this threshold, catabolism is the predominant elimination mechanism. Therefore, despite the >10,000-fold difference in sieving coefficients for 150 kDa proteins predicted by the two relationships (Supplementary Figure 3), both values are considered trivial and work similarly well for proteins with large MW. When

$MW < 30$ kDa, the two relationships almost converge (Supplementary Figure 3) and lead to very similar PK predictions. Accordingly, the discrepancy between these two relationships only becomes significant for molecules with MW ranging from 30–70 kDa. However, the present dataset contains few modalities of MW within this range in the dataset, and most of them are albumin or albumin-related proteins, which tend to align better with the sieving coefficient relationship developed by Sepp et al. that incorporates albumin. Therefore, as a rule of thumb, when using this two-pore PBPK model for a priori predictions of novel modalities with MW of 30–70 kDa, both sieving coefficient relationships can be utilized. The resulting simulations can be considered as lower and upper bounds of PK predictions, as demonstrated in Fig. 2F.

The difference between the two sieving coefficient relationships arises because the one developed by Sepp et al. is meant for neutral proteins and albumin [17, 30], whereas the one by Li and Shah applies to positively charged macromolecules [8, 19]. The negatively charged glycosaminoglycans on glomerular basement membrane hinder the filtration of proteins with negative charges [31], leading to lower θ for these proteins. And molecular charge impacts not only renal filtration (θ), but also nonspecific pinocytosis (CL_{up}) via electrostatic interactions with negatively charged cell membrane [37]. In particular, we found that the modeled pinocytosis of negatively charged albumin should be lower than other proteins, with the scale factor on the pinocytosis rate even lower in higher species ($Spino_{albumin, primate} < Spino_{albumin, rat} < Spino_{albumin, mouse} < 1$). This is consistent with the finding that pinocytosis of albumin in humans is about sixfold lower than that of albumin in mice in Sepp et al.'s two-pore model [17, 18]. The reasons for species-dependent $Spino$ for albumin may be three-fold. First, the isoelectric points for mouse, rat, and human serum albumin are reported to be 6.3 [67], 5.7 [68], and 4.8 [69], respectively. This suggests that albumins from higher species tend to be more negatively charged, and may have greater electrostatic repulsion from cell membrane decorated with dense negative charge and hence lower $Spino$. On top of that, the sensitivity of the nonspecific uptake rate in response to molecular charge may also differ among species. Last, we cannot exclude the possibility that paracellular and pinocytotic transport is inherently slower in higher species. Our model assumes consistent CL_{up} , fractional lymph flow rates, pore sizes, and pore abundancies across species. In contrast, several other two-pore models suggest that protein PK in higher species, especially humans, would be better described assuming a reduced fraction of lymph flow [15], slower convective transport, and slower endocytosis rate [57]. However, it is difficult to confidently reach the same conclusion based on the current datasets.

Although the present two-pore model attempts to explain the effect of charge on renal elimination and pinocytosis, we

did not systematically evaluate charge as an independent variable of protein PK by deriving continuous relationships between PK parameters and molecular charge, as done for MW. Nevertheless, as more disposition data of different-size protein charge variants becomes available, we aim to incorporate mechanisms such as charge-based renal filtration, pinocytosis, transcapillary transport, and nonspecific binding to extracellular matrix to establish a more comprehensive quantitative structure-PK relationship (QSPKR) for protein therapeutics [27, 70, 71].

Calibration of endogenous proteins

When PBPK systems incorporate an endogenous protein such as IgG, the most common approach is manually adjusting the production rate to match its known steady-state concentration [58]. However, this makes it impossible to run estimation of any parameters that impact the turnover of the endogenous substance, such as FcRn concentrations, FcRn binding affinities, and the protein degradation rate, when the synthesis rate is not certain. It would also become very tedious to try out different model structures during the model development, as the production rates of endogenous substances always need to be re-calibrated. Alternatively, we applied the novel method for initialization of steady states to allow the synthesis rate to autonomously stabilize at the value that leads to the desired endogenous protein level prior to dosing (Supplementary Figure 1) [26]. These auto-optimized values align well with literature description. In healthy humans, the IgG synthesis rate in the model ($K_{syn\text{enIgG}} \cdot V_{Plasma} = 4.7 \times 10^{-7} \frac{M}{h} \times 1.41L = 15,905 \frac{\text{nmol}}{\text{day}} = 2386 \frac{\text{mg}}{\text{day}}$) was 34.1 mg/kg/day for a 70 kg subject, in line with reported 25–36 mg/kg/day [72], and the albumin synthesis rate ($K_{syn\text{enAib}} \cdot V_{Plasma} = 8.1 \times 10^{-6} \frac{M}{h} \times 1.41L = 274104 \frac{\text{nmol}}{\text{day}} = 18.4 \frac{\text{g}}{\text{day}}$) corresponds to 0.26 g/kg/day, which is close to the reported range of 0.13–0.22 g/kg/day [50]. It was reported that the FHH patients with a β 2m mutation had IgG and albumin synthesis rates within the normal range [50], which is consistent with our finding (Table 3). In monkeys, the modeled IgG synthesis rate ($K_{syn\text{enIgG}} \cdot V_{Plasma} = 2.4 \times 10^{-6} \frac{M}{h} \times 0.0335L = 1930 \frac{\text{nmol}}{\text{day}}$) is similar to 1792 nmol/day utilized in another PBPK model [70]. For a 280 g rat, the modeled IgG synthesis rate ($K_{syn\text{enIgG}} \cdot V_{Plasma} = 2.4 \times 10^{-6} \frac{M}{h} \times 0.00116L = 66.8 \frac{\text{nmol}}{\text{day}} = 10 \frac{\text{mg}}{\text{day}}$) is roughly 36 mg/kg/day, corresponding to the measured values of 15–44 mg/kg/day [73], and the modeled albumin synthesis rate ($K_{syn\text{enAib}} \cdot V_{Plasma} = 9.3 \times 10^{-5} \frac{M}{h} \times 0.00116L = 2.6 \frac{\text{pmol}}{\text{day}}$) of 9.3 μ mol/kg/day also falls in the experimentally measured range of 5.4–15.4 μ mol/kg/day [74, 75]. In mice, the IgG synthesis rate we obtained ($K_{syn\text{enIgG}} \cdot V_{Plasma} = 4.3 \times 10^{-6} \frac{M}{h} \times 0.0001273885L = 0.013 \frac{\text{pmol}}{\text{day}}$) is equivalent to

0.468 μ mol/kg/day for a 28 g mouse, slightly higher than 0.132 μ mol/kg/day estimated in another model [76].

Limitations and future directions of the model

In the PBPK model presented here, we assume that sizes (r_L and r_S) and relative abundances (α_L and α_S) of large pores and small pores remain constant across all tissues. However, the literature has suggested tissue-specific pore sizes for kidney, liver, bone, spleen, gastrointestinal tract, and pancreas, as well as tissue-specific pore abundances for liver, bone, spleen, lung, muscle, and skin [11, 15, 17]. We found that the parsimonious one-size-fit-all assumption only negligibly influenced model outputs if any, and greatly simplified model equations for more widespread use. It should be cautioned that if tissue-specific pore sizes and abundances are to be adopted, X_j and X_p are no longer constants and should be expressed as secondary parameters, and reflection coefficients (σ_L^{SUB} and σ_S^{SUB}) should depend on pore sizes in addition to MW. Readers are referred to the original derivations for these expanded equations [16, 17, 19].

Although the two-pore framework was originally derived only for continuous endothelia (non-fenestrated and fenestrated) [11], protein PK in tissues with discontinuous capillaries such as pancreas, bone, liver, and spleen was still captured well in the present study. However, we have excluded brain PK data throughout, as the two-pore theory does not seem to readily apply to the brain. We have previously investigated the effect of protein MW on brain PK following systemic administration in rats, and unraveled a bell-shaped relationship between the brain/plasma AUC ratio and protein MW (peak at 50 kDa) [77]. This poorly understood phenomenon goes against the log linear relationships between biodistribution coefficients and MW observed for other tissues [9], and cannot be captured using the present model. Moreover, the effective pore radius of brain tight junctions is less than 1 nm [78, 79], which is much smaller compared to other organs and restricts entry of most protein therapeutics. Although several studies have modeled transvascular transport in the brain by fitting a very slow brain lymphatic flow rate [15, 17], the physiological relevance of this approach is unclear. Our laboratory has developed and evolved a one-pore brain PBPK model that incorporates endothelia consisting of blood-brain barrier (BBB) and blood-cerebrospinal fluid barrier (BCSFB), the extracellular fluid system including cerebrospinal fluid and interstitial fluid, parenchymal cells, and the perivascular space ([80] and a manuscript in submission). We anticipate that the size-dependent brain disposition may be

better explained by incorporating variable diffusion coefficients in the perivascular pathway of this brain PBPK model [81], which awaits further investigation.

The current model focuses on size-dependent disposition and FcRn interactions with albumin and natural Fc. Although the dataset employed here covers a great diversity of protein therapeutics, some important proteins cannot be readily described by this model, especially FcRn-binding engineering IgG variants such as YTE, YPY, and YQAY, and FcRn inhibitors. Modeling PK of these modalities requires understanding of FcRn turnover and intracellular trafficking [82, 83], differential FcRn binding affinities at pH 7.4 and at pH 6 [84], FcRn distribution at the cell surface and in the endosome [83, 84], and so on. Going forward we plan to incorporate these processes within the present two-pore PBPK model.

Conclusions

In summary, here we have presented the development and optimization of a translational two-pore PBPK model that incorporates MW-dependent tissue extravasation and renal filtration, FcRn binding to Fc and albumin, as well as competition for FcRn binding from endogenous IgG and albumin. The final model can simultaneously characterize plasma and tissue disposition of different-size proteins in mice, rats, monkeys, and humans reasonably well. The proteins in the dataset cover at least 15 types of modalities relevant in drug development across MW of 13–205 kDa with or without FcRn interactions. As such, we believe that this cross-modality, cross-species platform PBPK model can guide modality selection and optimization strategies for the development of protein therapeutics.

Supplementary Information The online version contains supplementary material available at <https://doi.org/10.1007/s10928-024-09922-x>.

Acknowledgements We would like to thank Drs. Veena Thomas and Isabel Figueroa for their great help in model development.

Author contributions Conceptualization: S.L., D.K.S.; Methodology: S.L., J.M.H., D.K.S.; Formal analysis and investigation: S.L., Y.L., Z.L., S.W.; Writing—original draft preparation: S.L.; Writing—review and editing: J.M.H., D.K.S.; Funding acquisition: D.K.S.; Supervision: D.K.S.

Funding The research work presented in this manuscript was supported by National Institute of General Medical Sciences grant [GM114179, GM146097], National Institute of Allergy and Infectious Diseases grant [AI138195], and National Cancer Institute grants [R01CA246785, R01CA256928, and R01CA275967].

Data availability No datasets were generated or analysed during the current study.

Declarations

Competing interests The authors declare no competing interests.

References

- Jin S et al (2022) Emerging new therapeutic antibody derivatives for cancer treatment. *Signal Transduct Target Ther* 7(1):39
- Zaman R et al (2019) Current strategies in extending half-lives of therapeutic proteins. *J Control Release* 301:176–189
- AlQahtani AD et al (2019) Strategies for the production of long-acting therapeutics and efficient drug delivery for cancer treatment. *Biomed Pharmacother* 113:108750
- Boswell CA et al (2010) Effects of charge on antibody tissue distribution and pharmacokinetics. *Bioconjug Chem* 21(12):2153–2163
- Li Z, Krippendorff BF, Shah DK (2017) Influence of Molecular size on the clearance of antibody fragments. *Pharm Res* 34(10):2131–2141
- Liu L (2015) Antibody glycosylation and its impact on the pharmacokinetics and pharmacodynamics of monoclonal antibodies and Fc-fusion proteins. *J Pharm Sci* 104(6):1866–1884
- Rafidi H et al (2021) Imaging reveals importance of shape and flexibility for glomerular filtration of biologics. *Mol Cancer Ther* 20(10):2008–2015
- Haraldsson B, Nystrom J, Deen WM (2008) Properties of the glomerular barrier and mechanisms of proteinuria. *Physiol Rev* 88(2):451–487
- Li Z et al (2016) Influence of molecular size on tissue distribution of antibody fragments. *MAbs* 8(1):113–119
- Rippe B, Haraldsson B (1987) Fluid and protein fluxes across small and large pores in the microvasculature. Application of two-pore equations. *Acta Physiol Scand* 131(3):411–28
- Rippe B, Haraldsson B (1994) Transport of macromolecules across microvascular walls: the two-pore theory. *Physiol Rev* 74(1):163–219
- Baxter LT et al (1995) Biodistribution of monoclonal antibodies: scale-up from mouse to human using a physiologically based pharmacokinetic model. *Cancer Res* 55(20):4611–4622
- Ferl GZ, Wu AM, DiStefano JJ 3rd (2005) A predictive model of therapeutic monoclonal antibody dynamics and regulation by the neonatal Fc receptor (FcRn). *Ann Biomed Eng* 33(11):1640–1652
- Davda JP et al (2008) A physiologically based pharmacokinetic (PBPK) model to characterize and predict the disposition of monoclonal antibody CC49 and its single chain Fv constructs. *Int Immunopharmacol* 8(3):401–413
- Niederla C et al (2018) A generic whole body physiologically based pharmacokinetic model for therapeutic proteins in PK-Sim. *J Pharmacokinet Pharmacodyn* 45(2):235–257
- Sepp A et al (2015) Development of a physiologically based pharmacokinetic model for a domain antibody in mice using the two-pore theory. *J Pharmacokinet Pharmacodyn* 42(2):97–109
- Sepp A et al (2019) Computer-assembled cross-species/cross-modalities two-pore physiologically based pharmacokinetic model for biologics in mice and rats. *J Pharmacokinet Pharmacodyn* 46(4):339–359
- Sepp A, Bergstrom M, Davies M (2020) Cross-species/cross-modality physiologically based pharmacokinetics for biologics: 89Zr-labelled albumin-binding domain antibody GSK3128349 in humans. *MAbs* 12(1):1832861
- Li Z, Shah DK (2019) Two-pore physiologically based pharmacokinetic model with de novo derived parameters for predicting plasma PK of different size protein therapeutics. *J Pharmacokinet Pharmacodyn* 46(3):305–318
- Li Z et al (2021) Two-pore physiologically based pharmacokinetic model validation using whole-body biodistribution of trastuzumab and different-size fragments in mice. *J Pharmacokinet Pharmacodyn* 48(5):743–762
- Li Z et al (2021) A two-pore physiologically based pharmacokinetic model to predict subcutaneously administered different-size antibody/antibody fragments. *AAPS J* 23(3):62

22. Kratz F (2008) Albumin as a drug carrier: design of prodrugs, drug conjugates and nanoparticles. *J Control Release* 132(3):171–183
23. Sleep D (2015) Albumin and its application in drug delivery. *Expert Opin Drug Deliv* 12(5):793–812
24. Baxter LT et al (1994) Physiologically based pharmacokinetic model for specific and nonspecific monoclonal antibodies and fragments in normal tissues and human tumor xenografts in nude mice. *Cancer Res* 54(6):1517–1528
25. Shah DK, Betts AM (2012) Towards a platform PBPK model to characterize the plasma and tissue disposition of monoclonal antibodies in preclinical species and human. *J Pharmacokinet Pharmacodyn* 39(1):67–86
26. Abuqayyas L, Harrold J (2015) A general method for initialization of steady-states in complex PK/PD systems. In: *Journal of pharmacokinetics and pharmacodynamics*, vol 42. Springer/plenum publishers, 233 Spring St, New York, NY 10013 USA, p S40
27. Hu S, D'Argenio DZ (2020) Predicting monoclonal antibody pharmacokinetics following subcutaneous administration via whole-body physiologically-based modeling. *J Pharmacokinet Pharmacodyn* 47(5):385–409
28. Chaudhury C et al (2006) Albumin binding to FcRn: distinct from the FcRn-IgG interaction. *Biochemistry* 45(15):4983–4990
29. Abdiche YN et al (2015) The neonatal Fc receptor (FcRn) binds independently to both sites of the IgG homodimer with identical affinity. *MAbs* 7(2):331–343
30. Lund U et al (2003) Glomerular filtration rate dependence of sieving of albumin and some neutral proteins in rat kidneys. *Am J Physiol Renal Physiol* 284(6):F1226–F1234
31. Gburek J, Konopska B, Golab K (2021) Renal handling of albumin—from early findings to current concepts. *Int J Mol Sci* 22(11):5809
32. Patlak CS, Goldstein DA, Hoffman JF (1963) The flow of solute and solvent across a two-membrane system. *J Theor Biol* 5(3):426–442
33. Gekle M (2005) Renal tubule albumin transport. *Annu Rev Physiol* 67:573–594
34. Tojo A, Kinugasa S (2012) Mechanisms of glomerular albumin filtration and tubular reabsorption. *Int J Nephrol* 2012:481520
35. Fan YY et al (2019) Human FcRn tissue expression profile and half-life in PBMCs. *Biomolecules* 9(8):373
36. D'Hooge L et al (2017) Cell surface dynamics and cellular distribution of endogenous FcRn. *PLoS One* 12(8):e0182695
37. Liu S et al (2021) Effect of variable domain charge on in vitro and in vivo disposition of monoclonal antibodies. *MAbs* 13(1):1993769
38. Zaias J et al (2009) Reference values for serum proteins of common laboratory rodent strains. *J Am Assoc Lab Anim Sci* 48(4):387–390
39. Gabrielsson J et al (2009) Early integration of pharmacokinetic and dynamic reasoning is essential for optimal development of lead compounds: strategic considerations. *Drug Discov Today* 14(7–8):358–372
40. Choi K et al (2016) Reference values of hematology, biochemistry, and blood type in cynomolgus monkeys from cambodia origin. *Lab Anim Res* 32(1):46–55
41. Schenk S et al (2008) A high confidence, manually validated human blood plasma protein reference set. *BMC Med Genomics* 1:41
42. Kang Y-k et al (2017) Glomerular filtration rate measurement in rats using F-18 sodium fluoride dynamic PET/CT: a single compartment model approach. *Soc Nuclear Med* 2017:524–524
43. Iwama R et al (2014) Estimation of glomerular filtration rate in cynomolgus monkeys (*Macaca fascicularis*). *J Vet Med Sci* 76(10):1423–1426
44. Wang Z, Wang G, Ren J (2022) Using a mathematical modeling to simulate pharmacokinetics and urinary glucose excretion of luseogliflozin and explore the role of SGLT1/2 in renal glucose reabsorption. *ACS Omega* 7(51):48427–48437
45. Garg A, Balthasar JP (2007) Physiologically-based pharmacokinetic (PBPK) model to predict IgG tissue kinetics in wild-type and FcRn-knockout mice. *J Pharmacokinet Pharmacodyn* 34(5):687–709
46. Cameron J et al (2016) Pharmacokinetic animal model. Google Patents
47. Hardiansyah D, Ng CM (2022) Minimal physiologically-based pharmacokinetic model to investigate the effect of charge on the pharmacokinetics of humanized anti-HCV-E2 IgG antibodies in sprague-Dawley rats. *Pharm Res* 39(3):481–496
48. Zhou J et al (2003) Generation of mutated variants of the human form of the MHC class I-related receptor, FcRn, with increased affinity for mouse immunoglobulin G. *J Mol Biol* 332(4):901–913
49. Wani MA et al (2006) Familial hypercatabolic hypoproteinemia caused by deficiency of the neonatal Fc receptor, FcRn, due to a mutant beta2-microglobulin gene. *Proc Natl Acad Sci U S A* 103(13):5084–5089
50. Waldmann TA, Terry WD (1990) Familial hypercatabolic hypoproteinemia. A disorder of endogenous catabolism of albumin and immunoglobulin. *J Clin Invest* 86(6):2093–8
51. Liu S et al (2023) Clinical validation of translational antibody PBPK model using tissue distribution data generated with (89) Zr-immuno-PET imaging. *J Pharmacokinet Pharmacodyn* 50(5):377–394
52. Harrold JM, Abraham AK (2014) Ubiquity: a framework for physiological/mechanism-based pharmacokinetic/pharmacodynamic model development and deployment. *J Pharmacokinet Pharmacodyn* 41(2):141–151
53. Wu S et al (2022) PBPK model for antibody disposition in mouse brain: validation using large-pore microdialysis data. *J Pharmacokinet Pharmacodyn* 49(6):579–592
54. Vegt E et al (2010) Renal toxicity of radiolabeled peptides and antibody fragments: mechanisms, impact on radionuclide therapy, and strategies for prevention. *J Nucl Med* 51(7):1049–1058
55. Meibohm B, Zhou H (2012) Characterizing the impact of renal impairment on the clinical pharmacology of biologics. *J Clin Pharmacol* 52(1 Suppl):S48–S62S
56. Glassman PM, Balthasar JP (2016) Physiologically-based pharmacokinetic modeling to predict the clinical pharmacokinetics of monoclonal antibodies. *J Pharmacokinet Pharmacodyn* 43(4):427–446
57. Hardiansyah D, Ng CM (2018) Two-pore minimum physiologically-based pharmacokinetic model to describe the disposition of therapeutic monoclonal IgG antibody in humans. *Pharm Res* 35(3):47
58. Chen Y, Balthasar JP (2012) Evaluation of a catenary PBPK model for predicting the in vivo disposition of mAbs engineered for high-affinity binding to FcRn. *AAPS J* 14(4):850–859
59. Fan YY et al (2016) Tissue expression profile of human neonatal Fc receptor (FcRn) in Tg32 transgenic mice. *MAbs* 8(5):848–853
60. Li T, Balthasar JP (2018) FcRn expression in wildtype mice, transgenic mice, and in human tissues. *Biomolecules* 8(4):115
61. Wisniewski JR et al (2016) In-depth quantitative analysis and comparison of the human hepatocyte and hepatoma cell line HepG2 proteomes. *J Proteomics* 136:234–247
62. Arzumanian VA, Kiseleva OI, Poverennaya EV (2021) The curious case of the HepG2 cell line: 40 years of expertise. *Int J Mol Sci* 22(23):13135
63. Gjolberg TT et al (2022) Biophysical differences in IgG1 Fc-based therapeutics relate to their cellular handling, interaction with FcRn and plasma half-life. *Commun Biol* 5(1):832
64. Unverdorben F et al (2016) Pharmacokinetic properties of IgG and various Fc fusion proteins in mice. *MAbs* 8(1):120–128

65. Suzuki T et al (2010) Importance of neonatal FcR in regulating the serum half-life of therapeutic proteins containing the Fc domain of human IgG1: a comparative study of the affinity of monoclonal antibodies and Fc-fusion proteins to human neonatal FcR. *J Immunol* 184(4):1968–1976
66. Suzuki T et al (2021) The influence of antibody engineering on Fc conformation and Fc receptor binding properties: analysis of FcRn-binding engineered antibodies and an Fc fusion protein. *MAbs* 13(1):1923366
67. Wagatsuma A et al (2001) Molecular properties and gene expression of albumin in the skeletal muscle following hindlimb immobilization in a shortened position. *Acta Neuropathol* 101(6):540–546
68. Spada A et al (2021) The uniqueness of albumin as a carrier in nanodrug delivery. *Mol Pharm* 18(5):1862–1894
69. Wiig H et al (2003) Effect of charge on interstitial distribution of albumin in rat dermis in vitro. *J Physiol* 550(Pt 2):505–514
70. Hu S, Datta-Mannan A, D'Argenio DZ (2022) Monoclonal antibody pharmacokinetics in cynomolgus monkeys following subcutaneous administration: physiologically based model predictions from physicochemical properties. *AAPS J* 25(1):5
71. Liu S, Shah DK (2023) Physiologically based pharmacokinetic modeling to characterize the effect of molecular charge on whole-body disposition of monoclonal antibodies. *AAPS J* 25(3):48
72. Waldmann TA, Strober W (1969) Metabolism of immunoglobulins. *Prog Allergy* 13:1–110
73. Cure SF, Cremer NE (1969) Decreased rate of synthesis of immunoglobulin (IgG) in rats infected with moloney leukemia virus. *J Immunol* 102(6):1345–1353
74. Gordon AH, Humphrey JH (1960) Methods for measuring rates of synthesis of albumin by the isolated perfused rat liver. *Biochem J* 75(2):240–247
75. Hoffenberg R, Gordon AH, Black EG (1971) Albumin synthesis by the perfused rat liver. A comparison of methods with special reference to the effect of dietary protein deprivation. *Biochem J* 122(2):129–34
76. Junghans RP (1997) IgG biosynthesis: no “immunoregulatory feedback.” *Blood* 90(10):3815–3818
77. Chang HY et al (2022) Effect of the size of protein therapeutics on brain pharmacokinetics following systematic administration. *AAPS J* 24(3):62
78. Sarin H (2010) Physiologic upper limits of pore size of different blood capillary types and another perspective on the dual pore theory of microvascular permeability. *J Angiogenes Res* 2:14
79. Zhang TT et al (2016) Strategies for transporting nanoparticles across the blood-brain barrier. *Biomater Sci* 4(2):219–229
80. Chang HY et al (2019) A translational platform PBPK model for antibody disposition in the brain. *J Pharmacokinet Pharmacodyn* 46(4):319–338
81. Pizzo ME et al (2018) Intrathecal antibody distribution in the rat brain: surface diffusion, perivascular transport and osmotic enhancement of delivery. *J Physiol* 596(3):445–475
82. Li T, Balthasar JP (2019) Application of physiologically based pharmacokinetic modeling to predict the effects of FcRn inhibitors in mice, rats, and monkeys. *J Pharm Sci* 108(1):701–713
83. de Witte WEA et al (2023) Mechanistic incorporation of FcRn binding in plasma and endosomes in a whole body PBPK model for large molecules. *J Pharmacokinet Pharmacodyn* 50(3):229–241
84. Jones HM et al (2019) A physiologically-based pharmacokinetic model for the prediction of monoclonal antibody pharmacokinetics from in vitro data. *CPT Pharmacometrics Syst Pharmacol* 8(10):738–747

Publisher's Note Springer Nature remains neutral with regard to jurisdictional claims in published maps and institutional affiliations.

Springer Nature or its licensor (e.g. a society or other partner) holds exclusive rights to this article under a publishing agreement with the author(s) or other rightsholder(s); author self-archiving of the accepted manuscript version of this article is solely governed by the terms of such publishing agreement and applicable law.